SANDIA REPORT
SAND2021-10785
Printed September 2021

FY21 Seismic Source Modeling Software Enhancements

Leiph Preston, Christian Poppeliers, and Mehdi Eliassi

Prepared by
Sandia National Laboratories
Albuquerque, New Mexico
87185 and Livermore,
California 94550

Issued by Sandia National Laboratories, operated for the United States Department of Energy by National Technology & Engineering Solutions of Sandia, LLC.

NOTICE: This report was prepared as an account of work sponsored by an agency of the United States Government. Neither the United States Government, nor any agency thereof, nor any of their employees, nor any of their contractors, subcontractors, or their employees, make any warranty, express or implied, or assume any legal liability or responsibility for the accuracy, completeness, or usefulness of any information, apparatus, product, or process disclosed, or represent that its use would not infringe privately owned rights. Reference herein to any specific commercial product, process, or service by trade name, trademark, manufacturer, or otherwise, does not necessarily constitute or imply its endorsement, recommendation, or favoring by the United States Government, any agency thereof, or any of their contractors or subcontractors. The views and opinions expressed herein do not necessarily state or reflect those of the United States Government, any agency thereof, or any of their contractors.

Printed in the United States of America. This report has been reproduced directly from the best available copy.

Available to DOE and DOE contractors from
U.S. Department of Energy
Office of Scientific and Technical Information
P.O. Box 62
Oak Ridge, TN 37831

Telephone: (865) 576-8401
Facsimile: (865) 576-5728
E-Mail: reports@osti.gov
Online ordering: http://www.osti.gov/scitech

Available to the public from
U.S. Department of Commerce
National Technical Information Service
5301 Shawnee Rd
Alexandria, VA 22312

Telephone: (800) 553-6847
Facsimile: (703) 605-6900
E-Mail: orders@ntis.gov
Online order: https://classic.ntis.gov/help/order-methods/

ABSTRACT

Seismic source modeling allows researchers both to simulate how a source that induces seismic waves interacts with the Earth to produce observed seismograms and, inversely, to infer what the time histories, sizes, and force distributions were for a seismic source given observed seismograms. In this report, we discuss improvements made in FY21 to our software as applies to both the forward and inverse seismic source modeling problems. For the forward portion of the problem, we have added the ability to use full 3-D nonlinear simulations by implementing 3-D time varying boundary conditions within Sandia's linear seismic code Parelasti. Secondly, on the inverse source modeling side, we have developed software that allows us to invert seismic gradiometer-derived observations in conjunction with standard translational motion seismic data to infer properties of the source that may improve characterization in certain circumstances. First, we describe the basic theory behind each software enhancement and then demonstrate the software in action with some simple examples.

ACKNOWLEDGEMENTS

The authors would like to acknowledge Lance Prothro for constructing the Geologic Framework Model that forms the basis of the 3-D model used in this report. Also, we thank Jennifer Harding for converting the Geologic Framework Model into the format needed for the linear seismic simulations shown herein. This research was funded by the National Nuclear Security Administration, Defense Nuclear Nonproliferation Research and Development (NNSA DNN R&D). The authors acknowledge important interdisciplinary collaboration with scientists and engineers from LANL, LLNL, MSTS, PNNL, and SNL. This paper describes objective technical results and analysis. Any subjective views or opinions that might be expressed in the paper do not necessarily represent the views of the U.S. Department of Energy or the United States Government.

CONTENTS

LIST OF FIGURES

This page left blank

ACRONYMS AND DEFINITIONS

Abbreviation	Definition
2-D	two dimensional
2D-C	two dimensional cylindrical
3-C	three component
3-D	three dimensional
cc	cubic centimeter
CPML	convolutional perfectly matched layer
E-W	east-west
FY21	fiscal year 2021
FY22	fiscal year 2022
g	gram
GF	Green’s function
Hz	Hertz
kg	kilogram
m	meter
N-S	north-south
P-wave	primary (compressional) wave
RMS	root mean square
s	second
S-wave	shear wave
TVBC	time varying boundary condition
Vp	P-wave velocity
Vs	S-wave velocity

This page left blank

1. INTRODUCTION

Modeling of seismic sources can involve simulating a source of energy or distributions of forces within the Earth that induces seismic waves, which propagate through the Earth and are recorded at seismic recorders. This aspect of seismic source modeling, the forward problem, can allow researchers to discern what the ground motion from some scenario source would look like and study how parameters of the source affect those observed ground motions. Seismic source representations can range from simple combinations of force couples acting at a point, which is a linear far-field approximation, to full nonlinear simulations of the energy source including material phase changes and shock wave propagation. It is well known that buried explosions nonlinearly deform the surrounding earth, causing fracturing and plastic deformation of the material. Thus, in order to study the effects of the source parameters and near-source environmental properties, it is proper to use a nonlinear algorithm to initially propagate the shock waves produced by an explosion. However, because of the complex physical equations that need to be solved in order to simulate explosions, nonlinear algorithms are much more computationally expensive compared to linear seismic algorithms (e.g. Preston et al., 2021). Therefore, it is computationally advantageous to switch to a linear seismic wave propagation algorithm once the propagating wavefield can be well approximated by linear elastic theory. In order to take advantage of the strengths of both nonlinear and linear algorithms, a coupling between the two types of algorithms is required. This report documents the implementation of 3-D time-varying boundary conditions (TVBC) in Sandia's linear elastic code Parelasti (Poppeliers and Preston, 2020). This TVBC allows a nonlinear algorithm such as CTH (Schmitt et al., 2017) to be used to initiate the source and propagate shock waves to the elastic radius, where by definition the waves can be well approximated as linear seismic waves, and recorded. These recordings can then be "played," in a sense, to drive linear wave motion within Parelasti to much farther distances than would be computationally feasible for nonlinear algorithms.

What we described above is the simulation of energy source to seismograms, or the forward modeling of the seismic source. The flip side, the inverse problem, involves using observed seismograms and inferring what distributions of forces, how big, and how those forces varied with time would optimally produce those observed seismograms. Often, in the inverse case, linear assumptions are made and the source is simplified by assuming that forces or force couples acting at a single point (or set of points) within the Earth can adequately predict observed ground motions. Additionally, it is often assumed that the observed seismograms can be written as a sum of convolutions of impulse responses (Green's functions; GF) with seismic source time functions (time evolution of source components) (e.g. Aki and Richards, 2002). Thus, for the inverse problem, nonlinear algorithms are not typically used primarily for simplicity, but these linear approximations are also generally quite good at replicating observations in practice (e.g. Poppeliers et al., 2020; Poppeliers and Preston, 2020; Preston et al., 2021). Although seismic source inversion theory is well developed for traditional translational motion seismic data, it is not as well understood for seismic gradiometer data, which is becoming more prevalent. This report also describes our new ability to utilize a combination of both traditional translational motion seismograms and gradiometer data to solve for the optimal seismic source model that matches the data.

First, we briefly describe the theory behind the 3-D TVBC implementation. Also, because the CTH simulations that we have done to date have assumed 2-D cylindrical symmetry (2D-C), we will describe how we translated 2D-C output from CTH to full 3-D TVBC information in order to test the 3-D TVBC implementation. Chapter 3 shows the operation of the 3-D TVBC within a simple 3-D Earth model, where the 2D-C assumption from the CTH simulations is still valid, and a second where a full 3-D model with topography demonstrates the full 3-D TVBC in action and also how the breaking of the 2D-C assumption from the CTH simulations induces some noise in the 3-D results that will be overcome once full 3-D CTH simulations are completed as part of FY22's work.

In Chapter 4 we describe the theory and implementation for incorporating gradiometer observations into full waveform seismic moment tensor solutions. Chapter 5 will then demonstrate full waveform moment tensor inversion using simulated gradiometer data within a 3-D Earth model first when using only translational and rotational motion data separately, and finally together in a joint inversion using both data types simultaneously.

2. 3-D TIME-VARYING BOUNDARY CONDITIONS

We first briefly describe the 3-D linear elastic full waveform simulation code, Parelasti, then we describe how the 3-D time-varying boundary conditions (TVBC) were implemented within Parelasti, and, finally, the conversion from 2-D cylindrical symmetry CTH tracer data to the 3-D information needed by the 3-D TVBC.

2.1. Parelasti

Parelasti solves the 3-D elasto-dynamic velocity-stress first-order set of partial differential equations:

$$\frac{\partial v_i(\mathbf{x},t)}{\partial t} = \frac{1}{\rho(\mathbf{x})}\left(\frac{\partial \sigma_{ij}(\mathbf{x},t)}{\partial x_j} + f_i(\mathbf{x},t)\right) \tag{2-1a}$$

$$\frac{\partial \sigma_{ij}(\mathbf{x},t)}{\partial t} = \lambda(\mathbf{x})\frac{\partial v_k(\mathbf{x},t)}{\partial x_k}\delta_{ij} + \mu(\mathbf{x})\left(\frac{\partial v_i(\mathbf{x},t)}{\partial x_j} + \frac{\partial v_j(\mathbf{x},t)}{\partial x_i}\right) + \frac{\partial m_{ij}(\mathbf{x},t)}{\partial t} \tag{2-1b}$$

where $v_i(\mathbf{x},t)$ is the i^{th} component of particle velocity (x, y, or z) at 3-D spatial location $\mathbf{x}$ and time t, $\rho(\mathbf{x})$ is material density, $\sigma_{ij}(\mathbf{x},t)$ is the (i,j) component of the 3x3 symmetric stress tensor, $f_i(\mathbf{x},t)$ is the time-varying body force source term in cartesian direction i, $\lambda(\mathbf{x})$ and $\mu(\mathbf{x})$ are the Lamé and shear moduli for an isotropic elastic medium, and $m_{ij}(\mathbf{x},t)$ is a time-varying moment tensor source term (e.g. Aki and Richards, 2002).

These partial differential equations are solved with a time-domain standard-staggered-grid finite-difference scheme using operators that are second-order accurate in time and fourth-order accurate in space. Specifically, compressive stress components are located at the corners of a unit cell, shear stresses are in the center of each face of the unit cell, and velocities are located at the mid-point of each edge of the unit cell (Figure 2-1, top). Velocity and stress component updates are also staggered in time, with stresses being updated on integer time steps and velocities at half-integer time steps (Figure 2-1, bottom). Medium parameters are stored coincident with compressive stress components (unit cell corners). Thus, densities and shear moduli must be interpolated to velocity

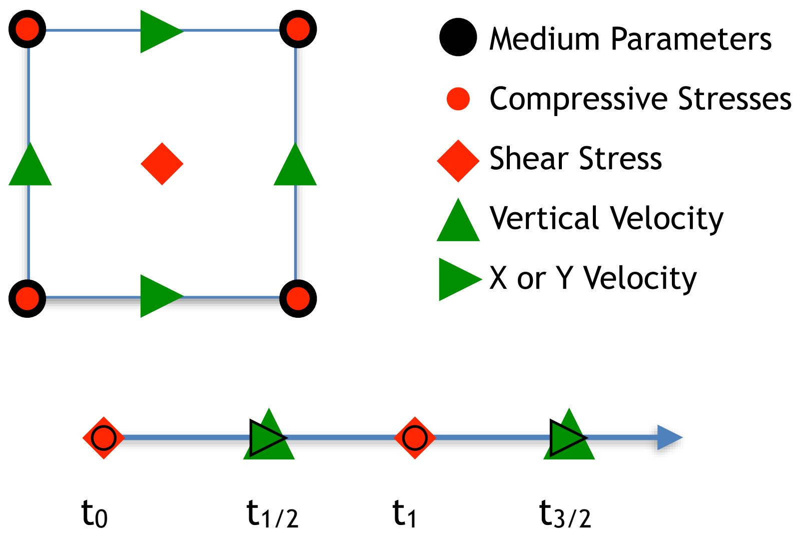

Figure 2-1: One face of a 3-D unit cell (top) and time updating (bottom) for the staggered finite-difference scheme.

and shear stress locations, respectively. Densities use simple linear interpolation onto velocity locations, but shear moduli use harmonic averaging of the surrounding four shear moduli to interpolate these onto the face-centered shear stress location (Moczo et al., 2002).

Seismic sources from a linear seismic source perspective can be introduced by specifying body force and/or moment tensor source terms as shown in Equations 2-1a,b above. These source terms can be any time variable function that has a frequency content supported by the grid discretization in order to minimize numerical dispersion in the simulations. One exception to this rule is impulse sources. An impulse source time function (first time sample non-zero, remaining time samples zero) can be used to produce Green's function (GF) or impulse response seismograms. Using GFs allows a wide variety of source time functions to be utilized with a single run of Parelasti and also allows full waveform moment tensor source inversions since these directly use GFs. A simple convolution of the GFs with a properly band-limited source time function produces identical results as if one had used that source time function to initialize Parelasti.

2.2. 3-D Time Varying Boundary Condition

The 3-D TVBC that is necessary for Parelasti is very similar to that described in Preston (2017) for the 2D-C code axiElasti given their similarities in storage locations and finite-difference stencils. The obvious difference is the addition of an extra dimension. Because Parelasti uses fourth order spatial finite-difference operators, at least three "layers" of information, one unit cell in width (*dh*) are required in all three spatial dimensions from the nonlinear output at all time steps in order to drive the wavefield within Parelasti (Figure 2-2). In order to update the compressive stress at point D in Parelasti (Figure 2-2) information from CTH (or any other algorithm) must be provided within the TVBC at velocity points A and C, along with information already available directly from Parelasti at velocity point E and the next velocity node off the image to the right. Similarly, to update the velocity at point E in Parelasti, compressive stress information from CTH at point B is required along with information already available from within Parelasti itself for compressive stresses at point D and two other points off the image to the right. Similar arguments go for velocities at point D and shear stresses at point E within Parelasti. Of course, updating at point D in Parelasti also requires information upward and downward in the image as well as in and out of the page for 3-D.

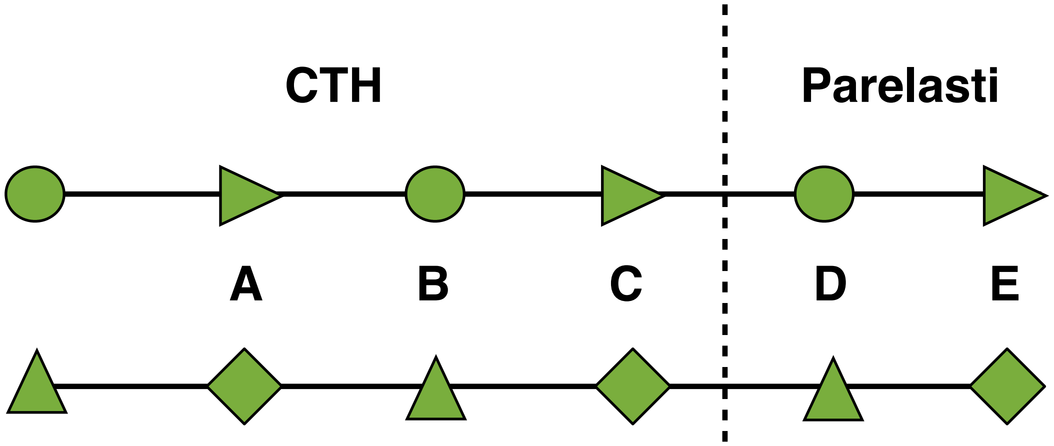

Figure 2-2: Required spatial distribution of velocities (triangles, right-pointing: horizontal velocities; upward-pointing: vertical velocities), compressive stresses (circles), and shear stresses (diamonds) needed by Parelasti from the CTH domain for time varying boundary conditions. Distance between A and C is *dh*.

Thus, velocity and stress information one and a half grid nodes away from the currently updating point must be available to Parelasti all three directions either from within Parelasti itself or provided to it from the TVBC. Instead of being a single layer boundary condition, it is better thought of as a rind surrounding the nonlinear source.

2.3. 2-D CTH output to 3-D TVBC

As mentioned in the introduction, we currently only have simulated nonlinear sources with the 2D-C version of CTH, primarily to save computational expense. Besides this, it allows us to test how well a 2D-C nonlinear simulation, which is much less expensive computationally than a 3-D nonlinear simulation, can do in a true 3-D environment. However, moving forward we will be utilizing CTH's full 3-D capability. Thus, development of a 3-D TVBC in Parelasti was a necessary prerequisite before we could do seismic simulations in full 3-D. Because of all this, we need to be able to translate CTH 2D-C output into the proper locations and thickness of TVBC for 3-D Parelasti. This is primarily a simple coordinate rotation, but the simple rind of thickness *dh* shown in Figure 2-2 is not adequate information from 2D-C CTH to provide all that is needed when a cylinder is swept in 3-D by rotating the 2D-C TVBC about the z-axis. This is due to the fact that Parelasti needs all three layers (1 *dh* thickness) of information shown in Figure 2-2 at all 3-D discretized points surrounding the TVBC. To meet this condition at all 3-D discrete points actually requires a rind of thickness 3 *dh* in the radial direction in the captured data from 2D-C CTH. However, 1 *dh* thickness in the vertical dimension is still sufficient. For completeness, translations from 2D-C CTH velocities and stresses to 3-D ones are shown below:

$$v_x(\mathbf{x},t) = v_r(\mathbf{r},t)\cos(\phi) \tag{2-2a}$$

$$v_y(\mathbf{x},t) = v_r(\mathbf{r},t)\sin(\phi) \tag{2-2b}$$

$$v_z(\mathbf{x},t) = v_z(\mathbf{r},t) \tag{2-2c}$$

$$\sigma_{xx}(\mathbf{x},t) = \sigma_{rr}(\mathbf{r},t)\cos^2(\phi) + \sigma_{\theta\theta}(\mathbf{r},t)\sin^2(\phi) \tag{2-2d}$$

$$\sigma_{yy}(\mathbf{x},t) = \sigma_{rr}(\mathbf{r},t)\sin^2(\phi) + \sigma_{\theta\theta}(\mathbf{r},t)\cos^2(\phi) \tag{2-2e}$$

$$\sigma_{zz}(\mathbf{x},t) = \sigma_{zz}(\mathbf{r},t) \tag{2-2f}$$

$$\sigma_{xy}(\mathbf{x},t) = \frac{1}{2}\sin(2\phi)\big(\sigma_{rr}(\mathbf{r},t) - \sigma_{\theta\theta}(\mathbf{r},t)\big) \tag{2-2g}$$

$$\sigma_{xz}(\mathbf{x},t) = \sigma_{rz}(\mathbf{r},t)\cos(\phi) \tag{2-2h}$$

$$\sigma_{yz}(\mathbf{x},t) = \sigma_{rz}(\mathbf{r},t)\sin(\phi) \tag{2-2i}$$

where **x** is a 3-D point, **r** is a 2-D cylindrical point, and ϕ is the angle in the horizontal plane of the 3-D point relative to the positive x-axis direction about the z-axis through the centroid of the source. Also, since $\sigma_{\theta\theta}$ is not directly provided by CTH, it must be computed from quantities that are provided, namely σ_{rr}, σ_{zz}, and pressure, p, via:

$$\sigma_{\theta\theta}(\mathbf{r},t) = -3p(\mathbf{r},t) - \sigma_{rr}(\mathbf{r},t) - \sigma_{zz}(\mathbf{r},t) \tag{2-3}$$

It should be noted that in a true 3-D environment, there will be a mismatch between what the TVBC derived from a 2D-C simulation of CTH and the 3-D wavefield computed from Parelasti due to 3-D effects. Because the TVBC is a hard boundary, meaning that Parelasti's current calculations have no effect on the TVBC values, artifacts in the form of reflections off the TVBC boundaries will occur. The closer the match between the CTH-derived TVBC values and those computed within Parelasti from the structure within the Parelasti model, the fewer artifacts and artificial reflections will occur off the TVBC interface. A perfect match between the values of the TVBC and that within Parelasti would make the TVBC appear like it does not even exist, meaning no artifacts would be produced from interactions with the TVBC interface.

3. 3-D TVBC DEMONSTRATION

In this chapter we demonstrate the 3-D TVBC in action in two scenarios. The first is within a 3-D model that has 2-D cylindrical symmetry so that the 2D-C CTH output is valid. This provides a verification of the 3-D TVBC with a nonlinear code driving the 3-D full waveform simulation within Parelasti. The second demonstration is using the 2D-C CTH output within a 3-D model with topography so that the 2D-C simulations results mismatch the conditions in the model. This will evaluate what level of error is introduced by using a much less computationally expensive 2-D nonlinear simulation within a 3-D model.

3.1. Cylindrically Symmetric 3-D Parelasti Model

In this section we will evaluate the 3-D TVBC described in Chapter 2 by using a 3-D model that adheres to the 2D-C assumption used in CTH to produce the TVBC values. In this simulation, 18 tons of COMPC-4 (1.6 g/cc density) is buried 250 m below the Earth's surface within homogeneous wet tuff with air above the surface. The CTH output is captured at a box placed at roughly 170 m distance from the source, both radially and in the plus and minus z-directions (Figure 3-1). For Parelasti, a 5 m grid node spacing was used to construct the 3-D Earth model with model domain extents of approximately 1000 m in all three coordinate directions, x, y, and z. The Parelasti Earth model was homogeneous with Vp=3278 m/s, Vs=1892 m/s and a density of 1950 kg/m^3.

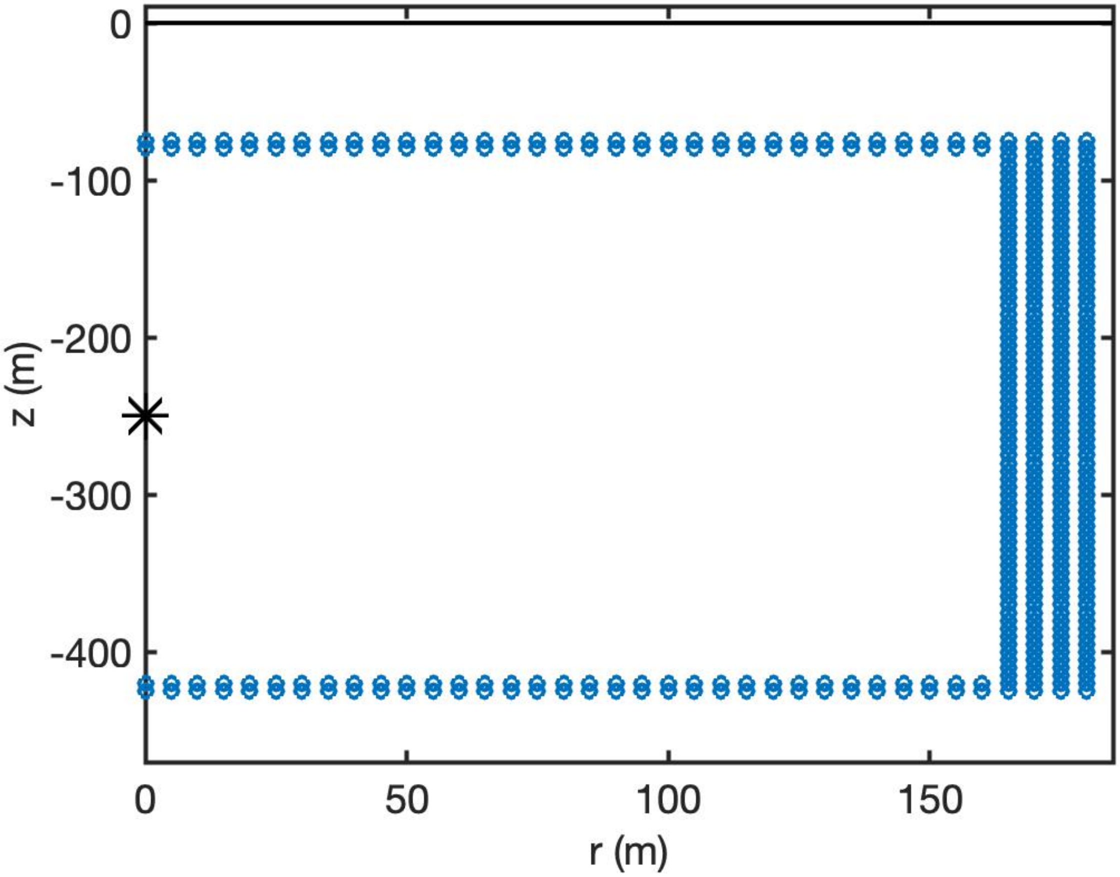

Figure 3-1: TVBC points captured in 2D-C CTH simulation. The black line at 0 m is the Earth's surface, asterisk denotes the centroid of the CTH source, and blue circles are TVBC locations.

We used a time step of 3e-5 s in Parelasti and simulated for 0.51 s. A low pass filter with corner of 17 Hz was applied to the CTH output before being used as a TVBC within Parelasti. Free-surface (zero normal stresses) boundary conditions (e.g. Aki and Richards, 2002) were applied at the top of the model to approximate the air-earth interface within Parelasti, and convolutional perfectly matched layer (CPML; Komatitsch and Martin, 2007) boundaries were applied on the other five sides of the model domain in order to mitigate artificial numerical reflections from the model boundaries. The CPML boundary damps the velocities near the edges of the domain, which causes the small velocity amplitudes seen near the sides of the following displayed wavefield snapshot images and is especially noticeable in the late time (0.5099 s) snapshots.

Figure 3-2a-c shows snapshots in time of the vertical particle velocity through the centroid of the source at three different times: 0.0809 s, 0.2222 s, and 0.5099 s post initiation of the detonation. At 0.0809 s, as expected, the P-wave front is just reaching the surface at z=0 m, and in 3-D forms two hemispheres: the up-going wavefront has upward particle velocity; the down-going wavefront has downward particle velocity with a nodal plane through the centroid of the source at z=250 m. Although in this cross-section, the TVBC appears as a rectangle, there are no obvious edge effects due to the TVBC. Because the TVBC points are hard conditions (i.e. Parelasti computations have no effect on their values) and completely surround the source region with no gaps, whatever happens inside the TVBC box stays inside the TVBC box and has no effect on results outside the box; hence, it is shown as a partially translucent box. Actually, some computational effort could be avoided by not computing anything inside the the TVBC volume because of this, and this savings will be implemented in the future.

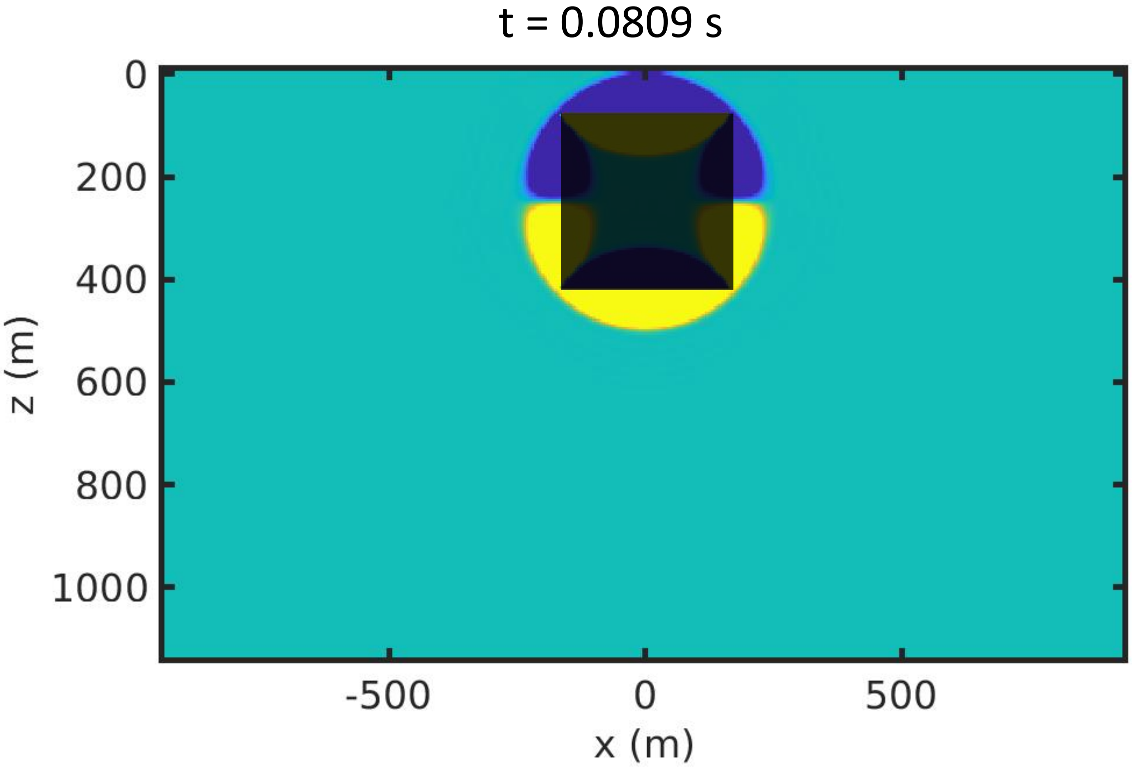

Figure 3-2a: Snapshot of vertical particle velocity at time 0.0809 s through the centroid of the source. Blue is upward particle motion; yellow is downward, and teal is near-zero vertical particle motion. Color saturates at about +/- 1% of peak particle velocity. The TVBC box is indicated as grey box. Values inside the TVBC box do not affect the wavefield external to the box.

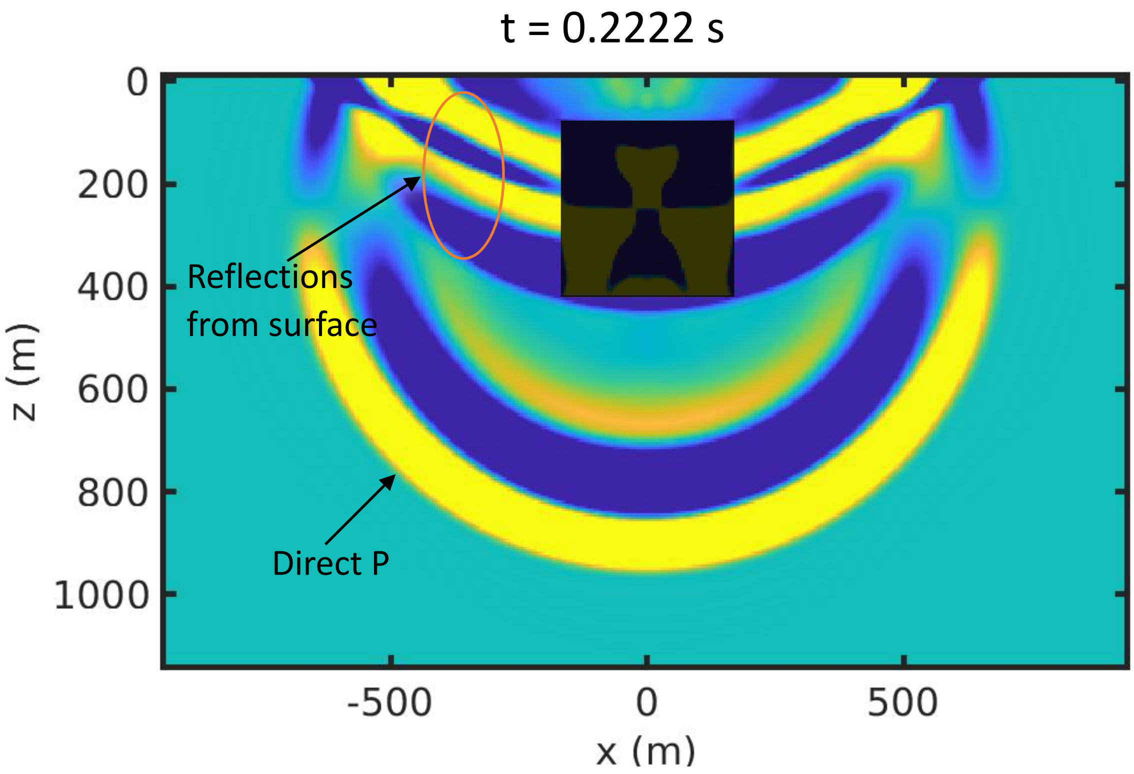

Figure 3-2b: Snapshot of vertical particle velocity at time 0.2222 s through the centroid of the source. Blue is upward particle motion; yellow is downward, and teal is near-zero vertical particle motion. Color saturates at about +/- 1% of peak particle velocity. The TVBC box is indicated as grey box. Values inside the TVBC box do not affect the wavefield external to the box. Main arrivals indicated by arrows and oval.

By 0.2222 s there is a clear reflection of the P-wave off the Earth's surface with the beginnings of other free-surface interaction effects such as converted S-waves and surface waves. There are perhaps some small artifacts of the TVBC between the top of the TVBC and the surface, but it is quite small given that the color saturates at approximately +/- 1% of peak particle velocity in these images. At 0.5099 s, the P-wave reflection has almost left the model domain with the P-to-S surface reflection being the dominant wavefront in the snapshot. Some small amplitude surface waves are also about to propagate off the left and right sides of the model domain. For comparison, in Figure 3-3 we show the same snapshot but using a point isotropic moment tensor source (i.e. no TVBC) with the source time function determined via linear source equivalent modeling (Preston et al., 2021) using only Parelasti for the entire simulation. In comparing the two snapshots, we see that near the TVBC box there are some artifacts that are quite small in amplitude, showing that there are some slight mismatches between the nonlinear and linear algorithms. However, given the completely different sets of equations solved, potential nonlinear effects that would be predicted by CTH but not Parelasti, and the different numerical implementations, the two codes are in remarkable agreement as shown by the very small amplitudes of these artifacts.

3.2. 3-D Parelasti Model

The prior section demonstrated excellent agreement between the CTH-produced TVBC values and the wavefield predicted by Parelasti when the 3-D Earth model is consistent with the 2D-C assumption made by the CTH simulation. This raises the question of how well and what level of artifacts are produced when the 3-D Earth model used in Parelasti does not conform to that

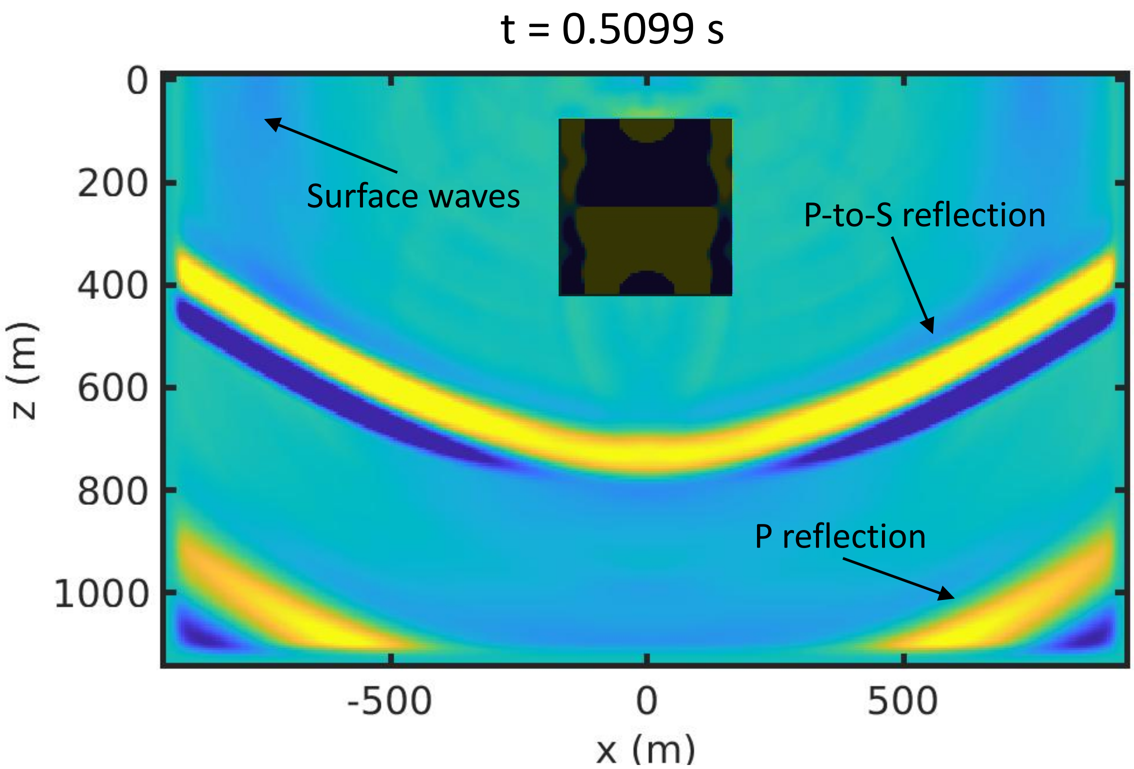

Figure 3-2c: Snapshot of vertical particle velocity at time 0.5099 s through the centroid of the source. Blue is upward particle motion; yellow is downward, and teal is near-zero vertical particle motion. Color saturates at about +/- 1% of peak particle velocity. The TVBC box is indicated as grey box. Values inside the TVBC box do not affect the wavefield external to the box. Main arrivals indicated by arrows.

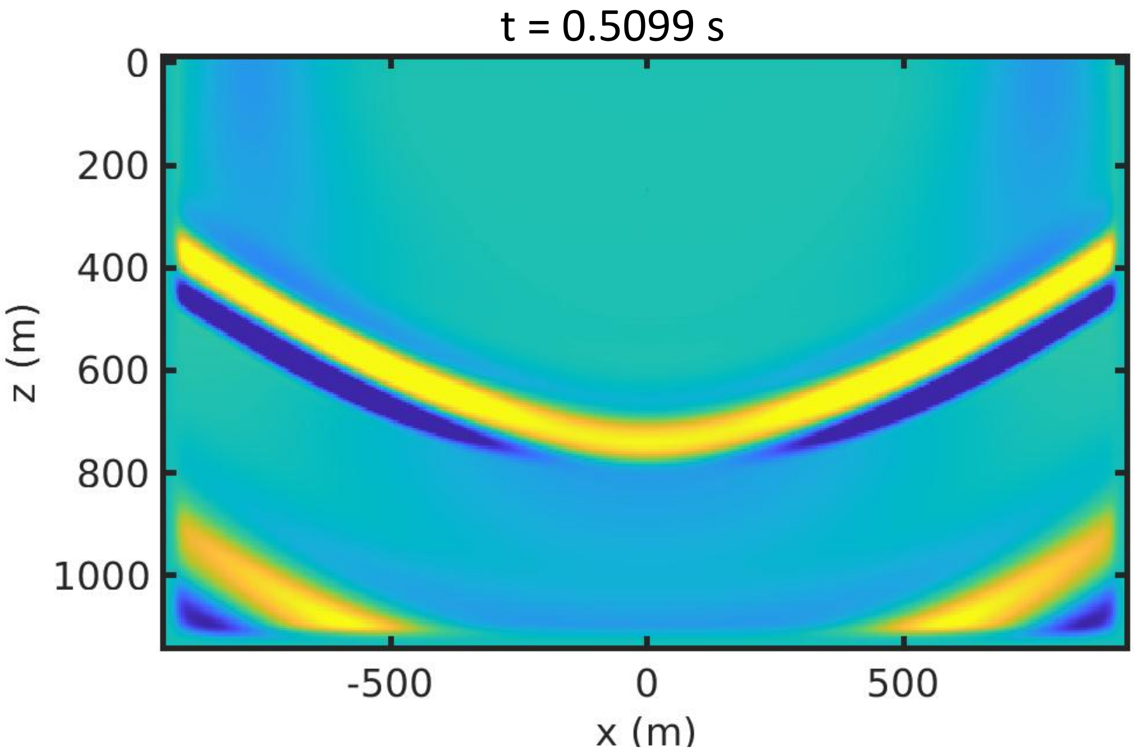

Figure 3-3: Snapshot of vertical particle velocity at time 0.5099 s through the source using point isotropic moment tensor source (no TVBC). Blue is upward particle motion; yellow is downward, and teal is near-zero vertical particle motion. Same relative color scale as in Figure 3-2c.

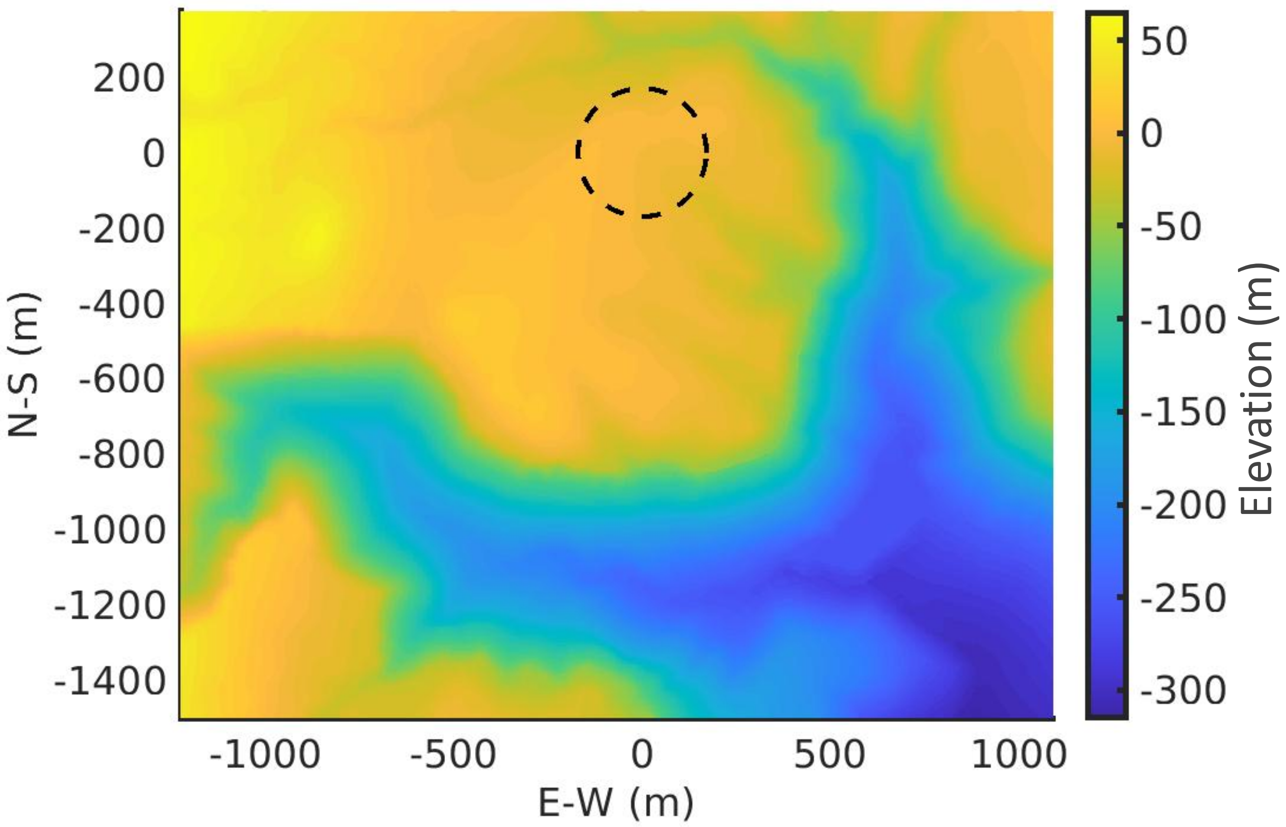

Figure 3-4: Topography of the 3-D Earth model with colorbar being height relative to elevation directly above the source at x = 0 m, y = 0 m. Dashed circle is the projection of the TVBC onto the surface.

assumption. For this test, we do not stray extremely far from the 2D-C assumption in that we still use the same homogeneous medium parameters within the solid Earth portion of the model as we did in the previous section. However, we do add topography to the model. Above the topography, we use uniform air properties of Vp=330 m/s and density of 1 kg/m^3. The topographic surface is shown in Figure 3-4, which has roughly 380 m of variation between the highest and lowest points of the model. The elevation of the topography directly above the source (x = 0 m, y = 0 m) is arbitrarily set to zero. Note that some topography lies below the source position in z. The TVBC cylinder is identical to that used in the previous section (Figure 3-1) and does not intersect the topographic surface at any point. Directly above the TVBC, the topography is relatively muted with about 10 m of variation (dashed circle in Figure 3-4). However, there are strong topographic variations by ~500 m from the source point.

Because of these topographic variations, 2-D cylindrical symmetry is no longer valid and artifacts are expected in the simulations that use the 2D-C CTH-derived TVBC. In Figures 3-5a-c we show snap shots of the vertical particle velocity wavefield at the same times as in the no-topography case. At 0.0809 s (Figure 3-5a), the P-wave front appears circular and is just reaching the topographic surface above the TVBC. Up to this point in time, the model has conformed to the 2D-C symmetry

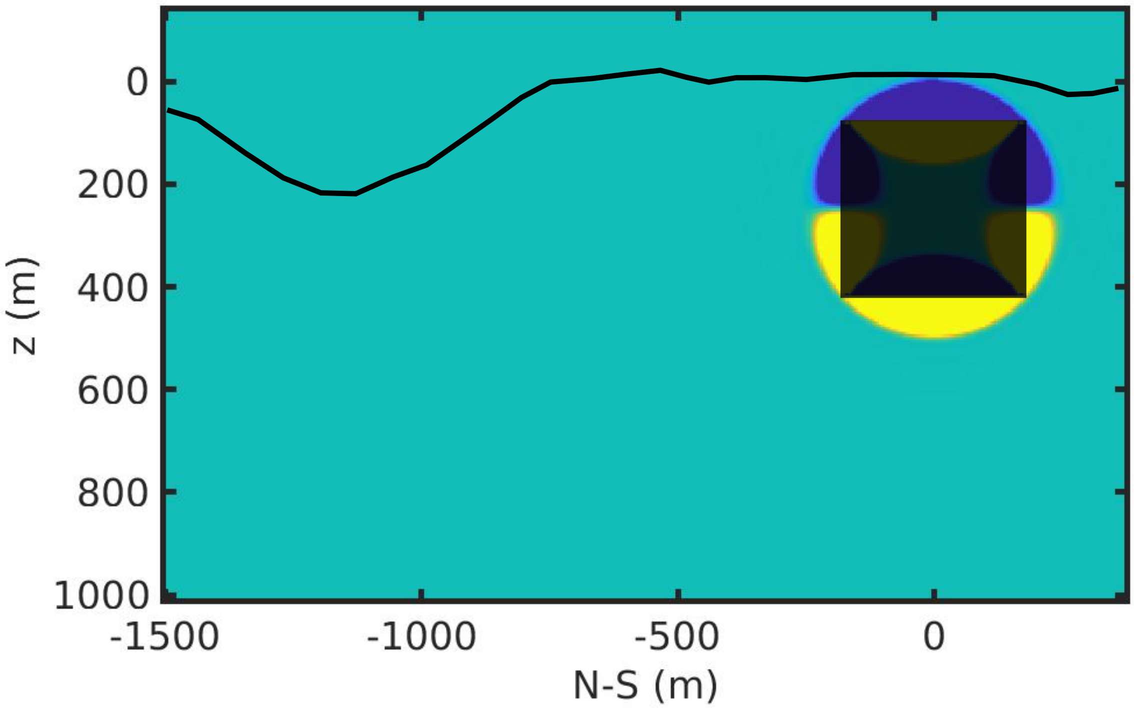

Figure 3-5a: Snapshot of vertical particle velocity at time 0.0809 s in a N-S cross-section through the centroid of the source. Blue is upward particle motion; yellow is downward, and teal is near-zero vertical particle motion. Color saturates at about +/- 1% of peak particle velocity. Topographic surface is indicated by black line. The TVBC box is indicated as grey box. Values inside the TVBC box do not affect the wavefield external to the box.

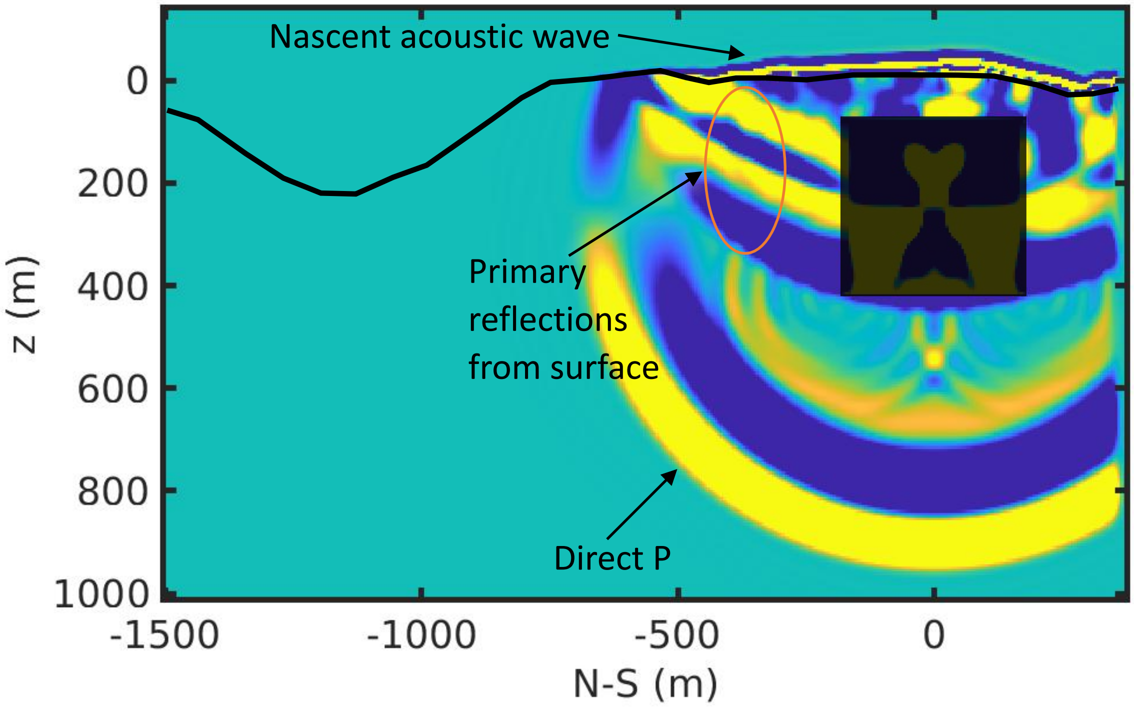

Figure 3-5b: Snapshot of vertical particle velocity at time 0.2222 s in a N-S cross-section through the centroid of the source. Blue is upward particle motion; yellow is downward, and teal is near-zero vertical particle motion. Color saturates at about +/- 1% of peak particle velocity. Topographic surface is indicated by black line The TVBC box is indicated as grey box. Values inside the TVBC box do not affect the wavefield external to the box. Main arrivals indicated by arrows and oval.

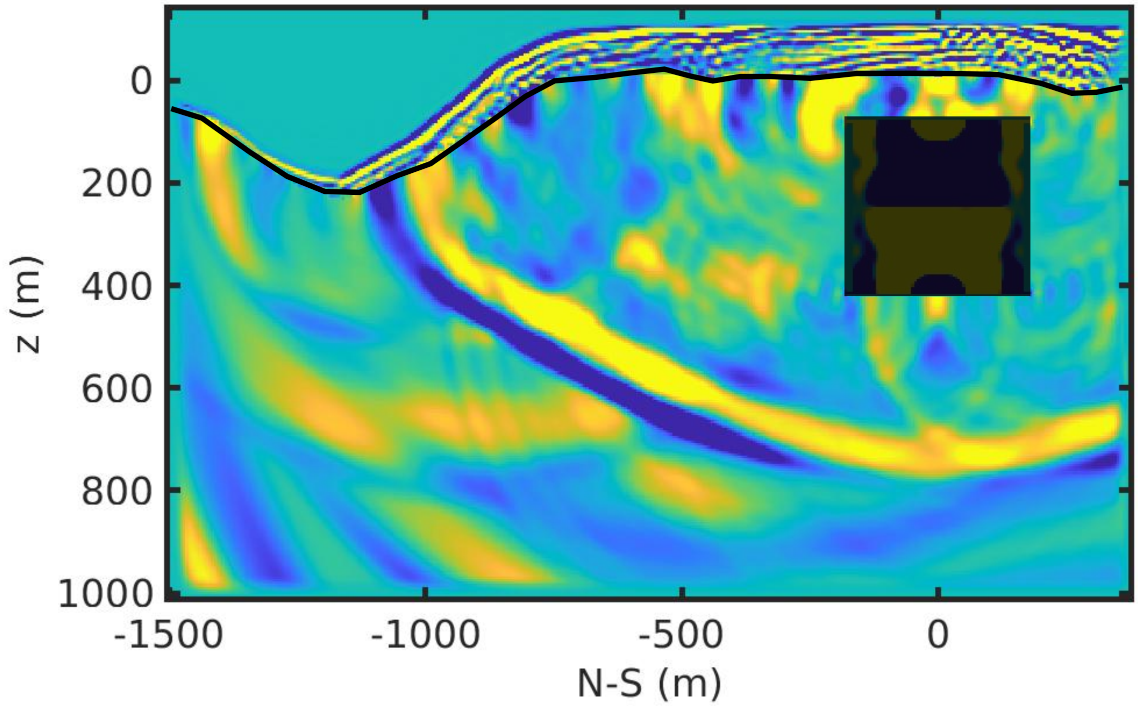

Figure 3-5c: Snapshot of vertical particle velocity at time 0.5099 s in a N-S cross-section through the centroid of the source. Blue is upward particle motion; yellow is downward, and teal is near-zero vertical particle motion. Color saturates at about +/- 1% of peak particle velocity. Topographic surface is indicated by black line. The TVBC box is indicated as grey box. Values inside the TVBC box do not affect the wavefield external to the box.

conditions. By 0.2222 s (Figure 3-5b) the wavefield has interacted with the topography and reflections from the surface are propagating downward in the earth and a nascent acoustic wave is propagating upward from the surface. Because of genuine 3-D effects, it is difficult to tell how much of the complexity above the TVBC box is artifact; however, below the TVBC there are some obvious artifacts between the direct P and surface reflected waves as some higher frequency waves can be seen that are clearly associated with the TVBC box, particularly with its corners. The 0.5099 s snap shot (Figure 3-5c) is obviously more complex than Figure 3-2c due to true 3-D topographic effects. However, there are artifacts clearly present especially, again, directly below the TVBC box.

To better distinguish TVBC artifacts from genuine 3-D structure, in Figures 3-6ab we show snap shots for t=0.2222 s and 0.5099 s for the case where we use a point source isotropic moment tensor with the same source time function we used in Section 3.1 (i.e. no TVBC). Since there is no TVBC box and the source time function is a linear equivalent source based upon the 2D-C CTH results, the wavefield from genuine 3-D effects should be very similar and the portions of Figures 3-5bc due to TVBC artifacts are readily apparent.

For 0.2222 s (Figure 3-5b compared to 3-6a), there are the obvious artifacts we discussed previously, but we can also see some differences in the wave fields directly above the TVBC box. The remainder of the wavefield is relatively unaffected by the TVBC box at this time. At 0.5099 s (Figure 3-5c compared with 3-6b), there are several artifacts present, primarily at a higher frequency than the genuine 3-D wavefield. However, major seismic phases are very similar between the two.

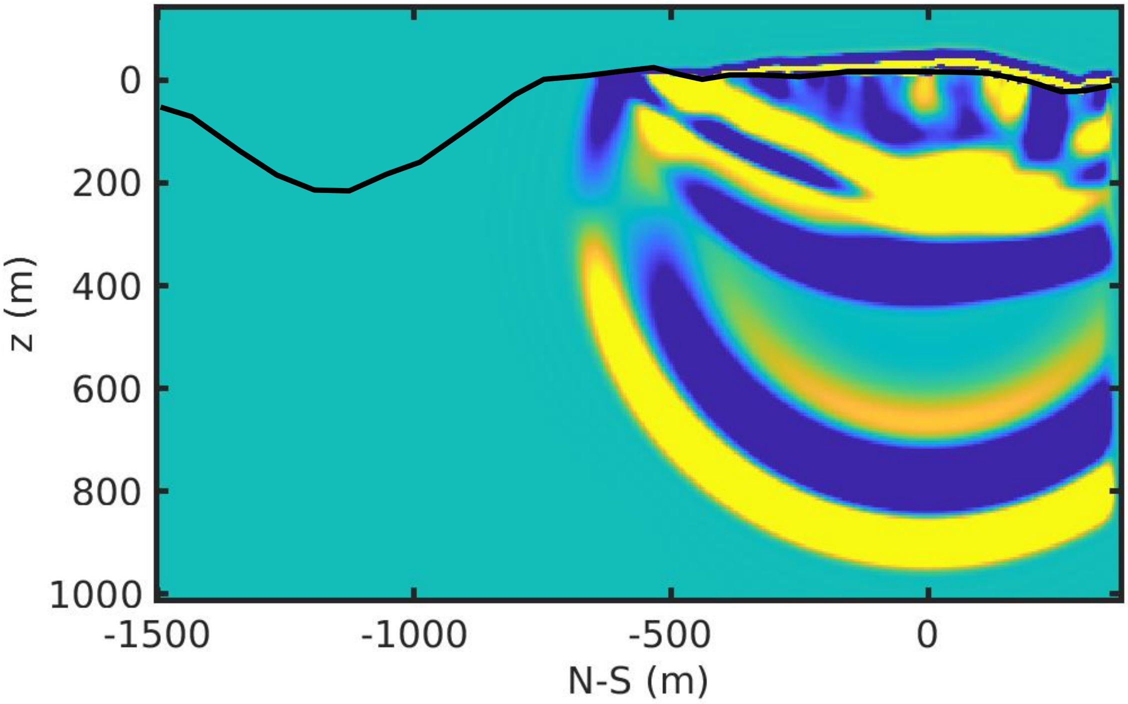

Figure 3-6a: Snapshot of vertical particle velocity at time 0.2222 s in a N-S cross-section through the source using point isotropic moment tensor. Blue is upward particle motion; yellow is downward, and teal is near-zero vertical particle motion. Color saturates at about +/- 1% of peak particle velocity. Topographic surface is indicated by black line.

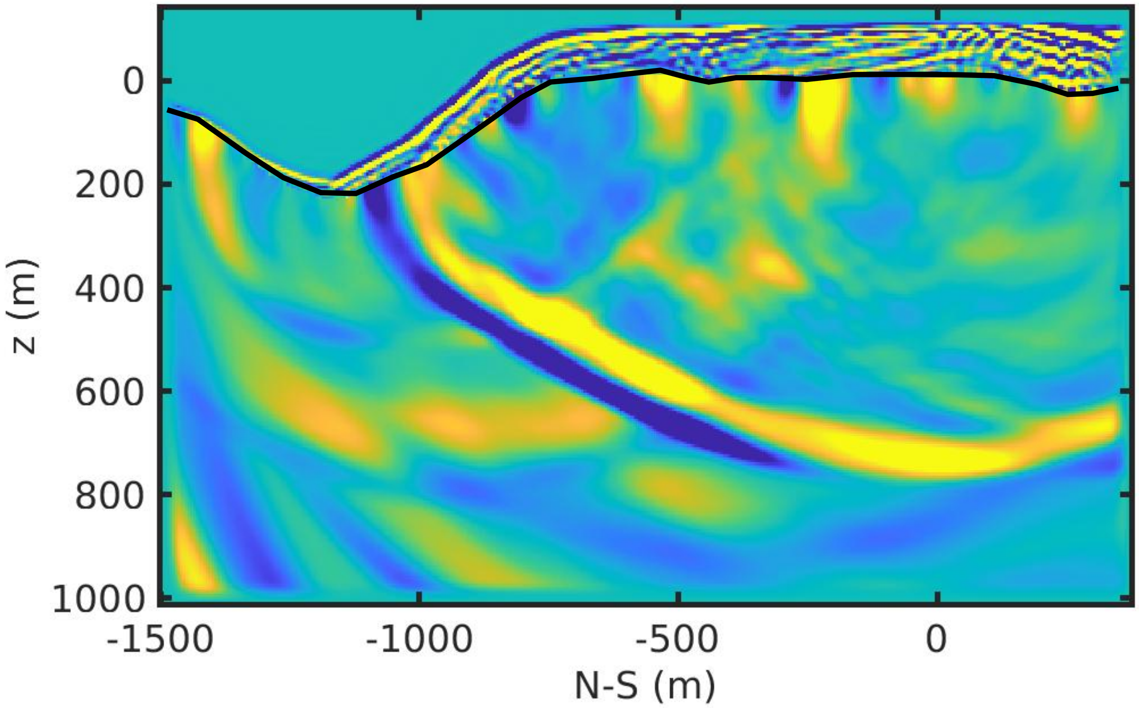

Figure 3-6b: Snapshot of vertical particle velocity at time 0.5099 s in a N-S cross-section through the source using a point isotropic moment tensor. Blue is upward particle motion; yellow is downward, and teal is near-zero vertical particle motion. Color saturates at about +/- 1% of peak particle velocity. Topographic surface is indicated by black line.

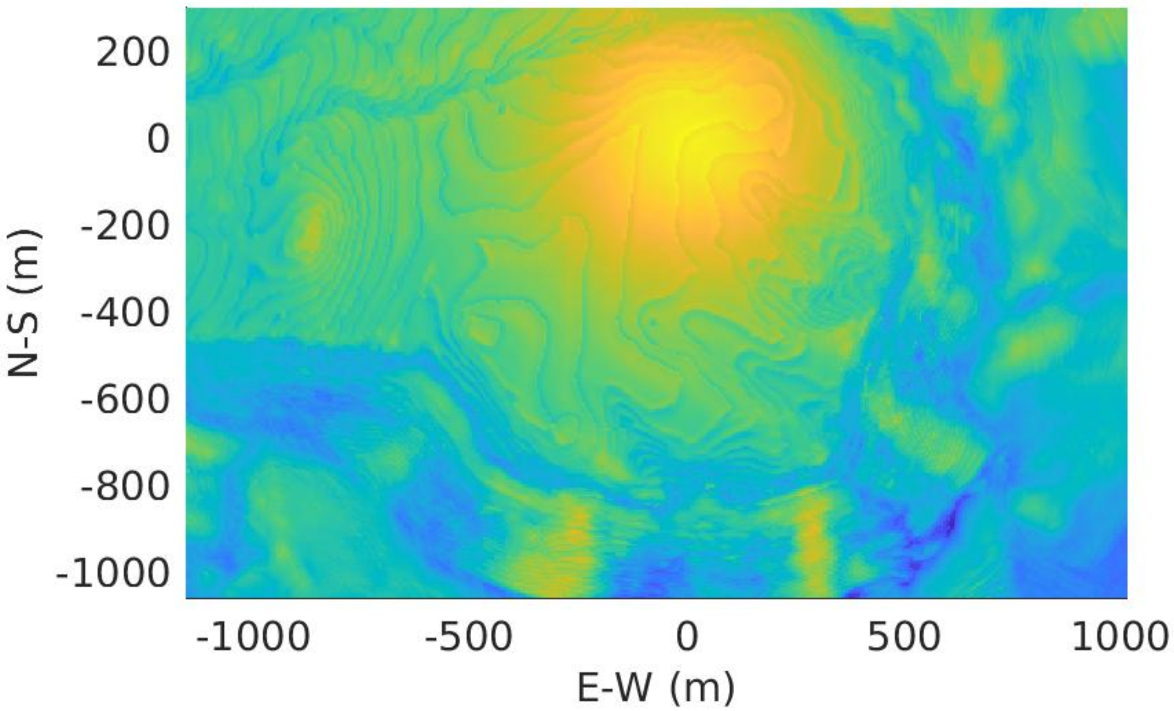

Figure 3-7: Log of peak vertical particle velocity at the earth's surface corrected for 1/r geometric spreading. Warm colors are higher peak velocities, while blues are lower velocities. (0,0) is the source location.

As a final example of the 3-D TVBC, the log of peak vertical particle velocity at the earth's surface corrected for 1/r geometric spreading is shown in Figure 3-7. Correcting for geometric spreading more clearly demonstrates the effects of topography on the wavefield, where warmer colors indicate areas that have larger relative amplitudes compared to 1/r spreading and blues are areas with lower than average amplitudes. Comparing with the topography shown in Figure 3-4 (note that Figure 3-7 covers a slightly smaller region than shown in Figure 3-4), we observe a clear correlation between topographic features and the peaks. The highest corrected particle velocities occur directly over the source region perhaps due somewhat to focusing effects from the local topography but also due to near- and intermediate-field terms given the proximity of the source and the predominate wavelengths in the simulation. Other than directly over the source, most other relative highs in the corrected particle velocities show strong correlation with local topographic effects such as small hills (e.g. at ~-800 m E-W, -200 m N-S) and ridges on the sides of the mesa. Relative lows tend to occur in the valleys and drainages.

This page left blank

4. GRADIOMETER THEORY

This chapter describes our developments and advances in seismic data inversion using a new type of seismic observation known as seismic gradiometry. Specifically, we describe a method to invert the entire seismic wavefield (consisting of the conventional translational ground motions as well as rotational motions) for a linear-equivalent seismic source model. Prior to this development, only the translational ground motions (e.g. one vertical and two horizontal components) were used.

The translational motion data that is typically used for this type of source estimation contains three degrees of freedom. However, this is only half the information in the seismic wavefield: by including the rotational motions of the wavefield, we are doubling the observable information. Indeed, there is evidence in the literature that including rotational motions in certain types of source-estimation inversions may increase the precision and resolution of the estimated seismic source parameters (Bernauer, et al., 2009; Bernauer and Fichtner, 2014; Reinwald et al., 2016; Donner et al., 2016; Ichinose et al., 2020); however, this previous work was only estimating a time-invariant seismic source model. For our work here, we describe a method to estimate the time variable seismic source, as may be more appropriate for explosion discrimination.

We begin by giving a brief overview of seismic gradiometry, how it is implemented, and the additional wavefield parameters that can be observed with it. We then review the forward model of far-field linear seismic waves and finally describe our inversion scheme using the full six-degrees-of-freedom wavefield (i.e. both translational and rotational motions).

4.1. Seismic Gradiometry

Seismic gradiometry refers to the process of estimating the time-varying spatial gradients of the seismic wavefield using a small scale seismic array. The theory was initially discussed in the context of linear and two dimensional seismic arrays by Langston (2007a,b,c) and extended to three dimensions by Poppeliers et al. (2013) and Poppeliers and Punosevac (2013), with applications and improvements described by Liang and Langton (2009) and Poppeliers (2010, 2011).

The method is founded on the model of a propagating seismic wave, that may contain geometrical spreading $G(r)$ and wave slowness $\mathbf{p}$, that might change with distance:

$$u(\mathbf{r}, t) = G(\mathbf{r}) f\left(t - \mathbf{p}(\mathbf{r} - \mathbf{r_0})\right)$$

where $\mathbf{r}$ is the position vector and $\mathbf{r_0}$ is the reference position. The derivative with respect to the spatial variable (i.e. the spatial gradient) is

$$\frac{\partial u}{\partial \mathbf{r}} = \mathbf{A}u + \mathbf{B}\frac{\partial u}{\partial t} \tag{4-1}$$

where the coefficient $\mathbf{A}$ relates to the geometrical spreading

$$\mathbf{A} = \frac{1}{G(r)}\frac{\partial G(r)}{\partial r} \tag{4-2}$$

and $\mathbf{B}$ relates to the wave slowness

$$\mathbf{B} = -\mathbf{p} - \frac{\partial \mathbf{p}}{\partial \mathbf{r}}(\mathbf{r} - \mathbf{r_0}) \tag{4-3}$$

There are several methods of solving Equations 4-2 and 4-3 for the attributes $\mathbf{A}$ and $\mathbf{B}$, but that is not our primary interest here. Rather, we note that any method of estimating $\mathbf{A}$ and $\mathbf{B}$ requires two quantities: the time and space derivatives of the wavefield. The temporal derivative of the seismic motion (i.e. the particle velocity) is directly measured by conventional seismic instrumentation.

However, estimating the spatial derivative essentially involves measuring small wavefield differences as a function of space.

A seismic gradiometer is type of seismic array that is designed specifically to estimate the spatial gradient of the wavefield. The primary requirements are that the instruments are well-calibrated and that the nominal aperture is small enough to measure the local slope of the wavefield, but large enough to not be unduly affected by instrument errors. Poppeliers and Evans (2015) developed a rule to optimize the aperture a of a surface-deployed gradiometer:

$$a = \frac{\xi}{\mathbf{p}f} \tag{4-4}$$

where $\mathbf{p}$ is the magnitude of the horizontal wave slowness, f is wave frequency, and ξ should be in the range of 0.03 to 0.08. A physical interpretation of ξ is that it represents the range of fractional wavelengths for which a gradiometer can accurately estimate the spatial gradients. Ideally, a gradiometer should consist of at least five seismometers (typically 3-C instruments) deployed in a circular array, where the ground material is relatively similar over the aperture of the array.

Seismic gradiometric analysis requires measurements of the displacement wavefield. As stated earlier, the temporal derivative of the wavefield (Equation 4-1) is simply the velocity seismogram, which is directly observed by most modern seismometers. To estimate the spatial gradient of the displacement wavefield, we employ a Taylor series, which gives the spatial gradient of the displacement wavefield du_i at a specific point in time at location $\mathbf{r}_i = (x_i, y_i)$ relative to a reference station, located at $\mathbf{r}_0 = (x_0, y_0)$ as

$$du_i = u_i - u_0 = \delta x_i \frac{\partial u}{\partial x}\bigg|_{\mathbf{r_0}} + \delta y_i \frac{\partial u}{\partial y}\bigg|_{\mathbf{r_0}} + du_i^{err} \tag{4-5}$$

where $\delta x_i = x_i - x_0, \delta y_i = y_i - y_0$ and du_i^{err} is a term accounting for the truncation error of the infinite Taylor series. So long as the conditions of Equation 4-4 are met, then we can ignore the error du_i^{err}. For a collection of N surface-mounted seismometers, all on a common time base, we can rewrite Equation 4-5 as a set of linear equations:

$$\begin{bmatrix} u_1 - u_0 \\ u_2 - u_0 \\ \vdots \\ u_N - u_0 \end{bmatrix} \approx \begin{bmatrix} (x_1 - x_0) & (y_1 - y_0) \\ (x_2 - x_0) & (y_2 - y_0) \\ \vdots & \vdots \\ (x_N - x_0) & (y_N - y_0) \end{bmatrix} \begin{bmatrix} (\frac{\partial u}{\partial x}) \\ (\frac{\partial u}{\partial y}) \end{bmatrix} \tag{4-6}$$

where the coordinates of the reference station are (x_0, y_0), (x_i, y_i) are the coordinates of the N supporting stations, and $u_i - u_0$ is the difference in the displacement seismogram between the supporting and reference stations, respectively, and the spatial gradients of the wavefield are $\frac{\partial u}{\partial x}$ and $\frac{\partial u}{\partial y}$. Equation 4-6 can be written as:

$$\mathbf{u} = \mathbf{R}\mathbf{g} \tag{4-7}$$

where $\mathbf{u}$ is a $1 \times N$ column vector of wavefield differences, $\mathbf{R}$ is the gradiometer geometry, and $\mathbf{g}$ is a 2×1 vector containing the spatial gradients and solved using generalized least squares. The gradients are estimated for every time point along the seismogram and Equation 4-7 can be solved using any component of data: i.e. for 3-C data, Equation 4-7 is constructed three times, once for each component of data, for every time point along the seismogram. Thus, the spatial gradients, $\frac{\partial u}{\partial x}$ and $\frac{\partial u}{\partial y}$, are time series. Finally, we emphasize that the data type for gradiometric analysis are displacement seismograms. Thus, the raw velocity seismograms as estimated by conventional seismometers must be converted to displacement using a numerical integration method prior to computing the seismic spatial gradients.

The rotational motions of the seismic wavefield are given by the curl of the displacement:

$$\Omega(\mathbf{r}', t) = \nabla \times \mathbf{u}(\mathbf{r}', t) \tag{4-8}$$

which gives

$$\Omega(\mathbf{r}', t) = \begin{bmatrix} \omega_x(\mathbf{r}', t) \\ \omega_y(\mathbf{r}', t) \\ \omega_z(\mathbf{r}', t) \end{bmatrix} = \begin{bmatrix} \frac{\partial u_z(\mathbf{r}', t)}{\partial y} - \frac{\partial u_y(\mathbf{r}', t)}{\partial z} \\ \frac{\partial u_x(\mathbf{r}', t)}{\partial z} - \frac{\partial u_z(\mathbf{r}', t)}{\partial x} \\ \frac{\partial u_y(\mathbf{r}', t)}{\partial x} - \frac{\partial u_x(\mathbf{r}', t)}{\partial y} \end{bmatrix} \tag{4-9}$$

The terms on the right hand side of Equation 4-9 are the spatial gradients of the wavefield, which are estimated using a gradiometer and solving Equation 4-7.

4.2. Inverse Method

The inversion is founded on a linear model for seismograms

$$u_k(\mathbf{r}', t') = \sum_{n=1}^{N_s} \int_{-\infty}^{\infty} g_{kn}(\mathbf{r}', t'; \mathbf{r}, t) m_n(\mathbf{r}, t)\, dt \tag{4-10}$$

where u_k is the seismogram for channel k, located at observation point $\mathbf{r}'$, m_n is a series of force couples acting at point $\mathbf{r}$, and g_{kn} are a series of seismic Green's functions (GFs) describing the impulse response from source n located at point $\mathbf{r}$ to the receiver located at $\mathbf{r}'$ (e.g. Stump and Johnson, 1977). Note that this linear model of seismograms is completely general, in that the GFs can describe any elastic wave type, be they P, S, or surface waves, as well as any type of seismic motion, translational or rotational. The only requirement is that the GFs explicitly predict the type of wave motion observed for channel k.

The goal of the work presented in this chapter and the next is to use the model in Equation 4-10 to estimate the parameters of the seismic source $m_n(\mathbf{r}, t)$. For analyzing a seismic wavefield produced by a buried explosion, we typically make a simplifying assumption that the seismic motion observed in the far field (i.e. at least several tens of wavelengths between the source and receiver) is a result of a series of forces and/or force couples acting at a point. For this model, $m_n(\mathbf{r}, t)$ is a 3x3 tensor that quantifies the nine possible force couples acting at point , which because of symmetry, contains only six independent terms, ($N_s = 6$ in Equation 4-10). The force couples contained in the tensor $m_n(\mathbf{r}, t)$ are time variable, and thus

$$m_n(\mathbf{r}, t) \rightarrow m_{ij}(\mathbf{r}, t) = \begin{bmatrix} M_{xx}(t) & M_{xy}(t) & M_{xz}(t) \\ M_{yx}(t) & M_{yy}(t) & M_{yz}(t) \\ M_{zx}(t) & M_{zy}(t) & M_{zz}(t) \end{bmatrix} \tag{4-11}$$

where $M_{ij} = M_{ji}$. Each term in $m_{ij}(\mathbf{r}, t)$ is a source time function that corresponds to a given component of the moment tensor (Aki and Richards, 2002).

By Fourier transforming Equation 4-1 into the frequency domain, the convolution becomes a multiplication,

$$U_k(\mathbf{r}', f) = \sum_{n=1}^{N_s} G_{kn}(\mathbf{r}', f; \mathbf{r}, f) M_n(\mathbf{r}, f) \tag{4-12}$$

which in matrix form can be written as

$$\mathbf{u} = \mathbf{Gm} \tag{4-13}$$

For Q frequencies, six independent source terms, and K receiver channels, Equation 4-13 is explicitly

$$\begin{bmatrix} \begin{pmatrix} | \\ U_1(f) \\ | \end{pmatrix} \\ \begin{pmatrix} | \\ U_2(f) \\ | \end{pmatrix} \\ \vdots \\ \vdots \\ \begin{pmatrix} | \\ U_K(f) \\ | \end{pmatrix} \end{bmatrix}_{KQ\times 1} = \begin{bmatrix} G_1^{(1)} & G_1^{(2)} & \cdots & G_1^{(6)} \\ G_2^{(1)} & G_2^{(2)} & \cdots & G_2^{(6)} \\ G_3^{(1)} & G_3^{(2)} & \cdots & G_3^{(6)} \\ \vdots & \vdots & \ddots & \vdots \\ G_K^{(1)} & G_K^{(2)} & \cdots & G_K^{(6)} \end{bmatrix}_{KQ\times 6Q} \begin{bmatrix} \begin{pmatrix} | \\ M_1(f) \\ | \end{pmatrix} \\ \begin{pmatrix} | \\ M_2(f) \\ | \end{pmatrix} \\ \vdots \\ \vdots \\ \begin{pmatrix} | \\ M_6(f) \\ | \end{pmatrix} \end{bmatrix}_{6Q\times 1} \tag{4-14}$$

where $\begin{bmatrix} - & U_k(f) & - \end{bmatrix}^T$ is a $Q \times 1$ column vector containing the frequency domain data for channel k, $\begin{bmatrix} - & M_n(f) & - \end{bmatrix}^T$ is the n^{th} frequency domain $Q \times 1$ column vector describing the source time function corresponding to the n^{th} component of the moment tensor, and

$$G_k^{(}i) = \begin{bmatrix} G_k^{(i)}(f_1) & \cdots & 0 \\ \vdots & \searrow & \vdots \\ 0 & \cdots & G_K^{(i)}(f_Q) \end{bmatrix}_{Q\times Q}$$

is the GF for the k^{th} receiver channel and the n^{th} moment tensor component.

Because the inversion is strictly linear, we can invert for each frequency individually, and concatenate the final results. Specifically, for frequency q,

$$\begin{bmatrix} U_1(f_q) \\ U_2(f_q) \\ \vdots \\ U_K(f_q) \end{bmatrix}_{K\times 1} = \begin{bmatrix} G_1^{(1)}(f_q) & G_1^{(2)}(f_q) & \cdots & G_1^{(6)}(f_q) \\ G_2^{(1)}(f_q) & G_2^{(2)}(f_q) & \cdots & G_2^{(6)}(f_q) \\ G_3^{(1)}(f_q) & G_3^{(2)}(f_q) & \cdots & G_3^{(6)}(f_q) \\ \vdots & \vdots & \ddots & \vdots \\ G_K^{(1)}(f_q) & G_K^{(2)}(f_q) & \cdots & G_K^{(6)}(f_q) \end{bmatrix}_{K\times 6} \begin{bmatrix} M_1(f_q) \\ M_2(f_q) \\ \vdots \\ M_6(f_q) \end{bmatrix}_{6\times 1} \tag{4-15}$$

Equation 4-15 is solved using generalized least squares

$$\mathbf{m} = \left(\mathbf{G}^T\mathbf{G}\right)^{-1}\mathbf{G}^T\mathbf{U} \tag{4-16}$$

where no damping or regularization is typically required. Note that the matrix in Equation 4-16 is solved for each frequency q individually. The results for all frequencies are therefore concatenated and converted to the time domain via the inverse Fourier transform. In previous work, the results are nearly identical whether we solve for all frequencies simultaneously, (Equation 4-14) or for each frequency separately (Equation 4-15) (see Figure 8 of Poppeliers et al., 2020).

The ordering of the data in Equation 4-15 and 4-16 is completely arbitrary, just so long as the appropriate GF is "matched" to the appropriate channel of data. Furthermore, the quantity u_k in Equation 4-10 (and Equations 4-14 through 4-16) can be any type of seismic motion. For example, a conventional seismometer records the ground velocity in three orthogonal directions

$$\mathbf{v}(\mathbf{r}', t) = \begin{bmatrix} v_x(\mathbf{r}', t) \\ v_y(\mathbf{r}', t) \\ v_z(\mathbf{r}', t) \end{bmatrix} \tag{4-17}$$

where the subscript indicates the component direction in a Cartesian coordinate system. Thus, the GFs used in Equation 4-10 to predict ground velocity will be velocity GFs and for typical three component data recorded by a traditional seismic array, the number of data channels (the variable K in Equations 4-14 and 4-15) will be three times the number of seismic stations (i.e. each seismic station will record three channels of data: v_x, v_y, and v_z). Likewise, the rotational motions (computed according to Equation 4-9),

$$\boldsymbol{\Omega}(\mathbf{r}', t) = \begin{bmatrix} \omega_x(\mathbf{r}', t) \\ \omega_y(\mathbf{r}', t) \\ \omega_z(\mathbf{r}', t) \end{bmatrix} \tag{4-18}$$

will have rotational GFs. To combine the translational velocity seismograms as well as the rotational motions, both data types are simply inserted into Equation 4-15 to form an augmented system of equations. For example we can arrange the two data types as,

$$\begin{bmatrix} \begin{pmatrix} | \\ v \\ | \end{pmatrix} \\ \begin{pmatrix} | \\ \Omega \\ | \end{pmatrix} \end{bmatrix} = \begin{bmatrix} \begin{pmatrix} | \\ G^{\{v\}} \\ | \end{pmatrix} \\ \begin{pmatrix} | \\ G^{\{\Omega\}} \\ | \end{pmatrix} \end{bmatrix} \mathbf{m} \tag{4-19}$$

where $[-\ \ v\ \ -]^T$ and $[-\ \ \Omega\ \ -]^T$ are column vectors that contain the velocity and rotational seismograms, respectively, $\left[-\ \ G^{\{v\}}\ \ -\right]^T$ and $\left[-\ \ G^{\{\Omega\}}\ \ -\right]^T$ are the corresponding velocity and rotational motion GFs, respectively, and **m** is a column vector that contains the seismic source parameters that we wish to estimate. Explicitly, Equation 4-19 could take the form

$$\begin{bmatrix} \begin{pmatrix} v_1(f_q) \\ v_2(f_q) \\ \vdots \\ v_K(f_q) \end{pmatrix} \\ \begin{pmatrix} \Omega_1(f_q) \\ \Omega_2(f_q) \\ \vdots \\ \Omega_L(f_q) \end{pmatrix} \end{bmatrix}_{(K+L)\times 1} = \begin{bmatrix} \begin{pmatrix} G_1^{\{v\}(1)}(f_q) & G_1^{\{v\}(2)}(f_q) & \cdots & G_1^{\{v\}(6)}(f_q) \\ G_2^{\{v\}(1)}(f_q) & G_2^{\{v\}(2)}(f_q) & \cdots & G_2^{\{v\}(6)}(f_q) \\ G_3^{\{v\}(1)}(f_q) & G_3^{\{v\}(2)}(f_q) & \cdots & G_3^{\{v\}(6)}(f_q) \\ \vdots & \vdots & \ddots & \vdots \\ G_K^{\{v\}(1)}(f_q) & G_K^{\{v\}(2)}(f_q) & \cdots & G_K^{\{v\}(6)}(f_q) \end{pmatrix} \\ \begin{pmatrix} G_1^{\{\Omega\}(1)}(f_q) & G_1^{\{\Omega\}(2)}(f_q) & \cdots & G_1^{\{\Omega\}(6)}(f_q) \\ G_2^{\{\Omega\}(1)}(f_q) & G_2^{\{\Omega\}(2)}(f_q) & \cdots & G_2^{\{\Omega\}(6)}(f_q) \\ G_3^{\{\Omega\}(1)}(f_q) & G_3^{\{\Omega\}(2)}(f_q) & \cdots & G_3^{\{\Omega\}(6)}(f_q) \\ \vdots & \vdots & \ddots & \vdots \\ G_L^{\{\Omega\}(1)}(f_q) & G_L^{\{\Omega\}(2)}(f_q) & \cdots & G_L^{\{\Omega\}(6)}(f_q) \end{pmatrix} \end{bmatrix}_{(K+L)\times 6} \begin{bmatrix} M_1(f_q) \\ M_2(f_q) \\ \vdots \\ M_6(f_q) \end{bmatrix}_{6\times 1} \tag{4-20}$$

for K channels of (velocity) translational data, L channels of rotational motion data, and frequency q. As written, Equation 4-20 shows the translational and rotational component data as distinct ‘blocks’. However, there is no need for this structure: the data can be arranged in blocks as shown here, or interleaved (e.g. one translational channel followed by one rotational channel, etc.). As mentioned previously, the ordering of the data in the matrix Equation 4-20 isn’t important, so long as the GFs correspond to the correct channel of data. This is due to the linearity of the problem, and numerical tests (some of which are presented in the next chapter) confirm this assertion.

5. GRADIOMETER DEMONSTRATION

In Chapter 4, we described the mathematical details of gradiometry, estimating rotational seismic motions using gradiometric analysis, and finally a linear inversion that's designed to estimate the time-varying moment tensor given both translational and rotational seismograms. In this chapter we discuss some of the implementation details as well as show some examples of inverting seismic data. The tests are synthetic throughout, and are designed only to demonstrate the validity of the mathematical model, as well as our implementation of the inversion scheme.

5.1. Synthetic Data

The data that we use to test our inversion here is synthetic throughout. Figure 5-1 shows the Earth model, as well as the array that we used to create the data. To create the data, we constructed a geologically reasonable model, defined a seismic source, and used a Sandia-developed, three-dimensional finite difference wavefield simulator to compute the seismograms (see Poppeliers and Preston, 2020 for details). The geologic model has a discrete spatial node spacing of 5 m, and the time step (Δt) that we used for the simulation was 0.00065 s. These finite difference parameters, along with the range of seismic wavespeeds in our model, allowed us to simulate wavefields up to approximately 20 Hz without significant numerical dispersion.

For the data, we define the source to simulate a buried explosion followed by a smaller release of tectonic strain. We simulate the source time functions for the buried explosion using the well-known Mueller-Murphy explosion source model (Haskel, 1967; Murphy, 1977; Mueller and Murphy, 1971). Specifically,

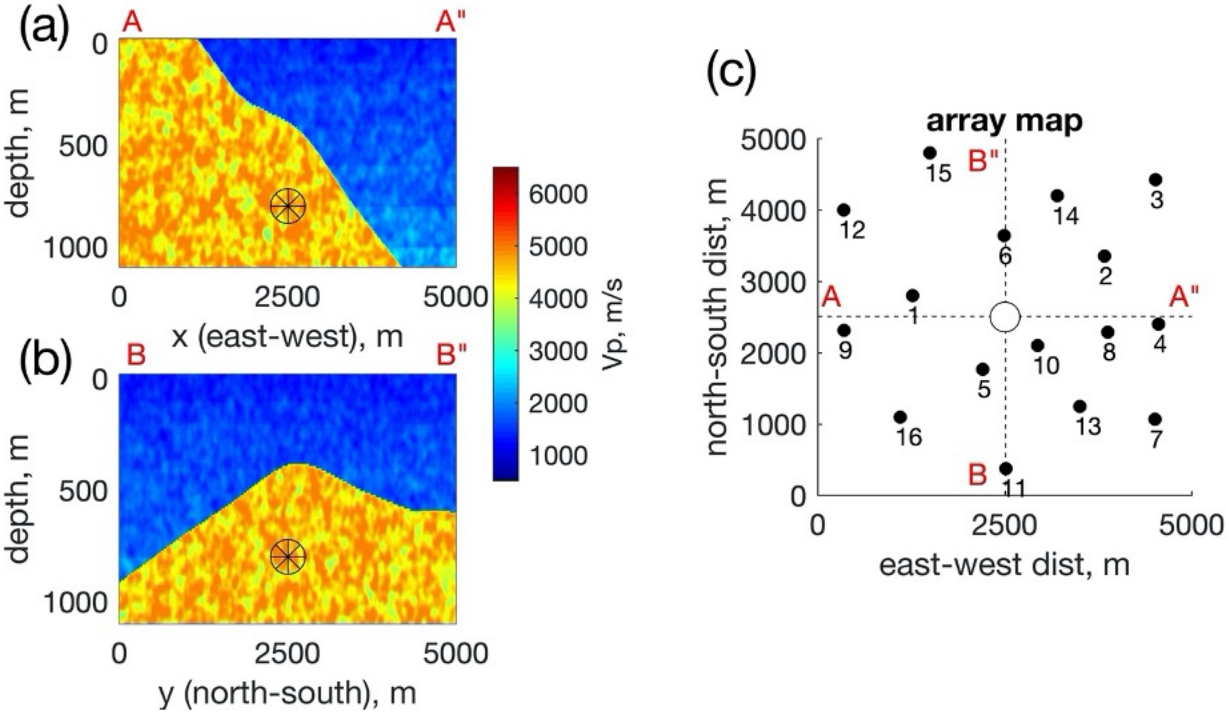

Figure 5-1: The geologic model and array stations used to test our inversion method. Panels (a) and (b) are orthogonal cross sections though the three-dimensional Earth model that we constructed, where the black circle at m is the source location. Panel (c) shows the surface location of the array stations used for our tests. At each numbered station, we collect three 3-C translational velocity seismograms, as well as three 3-C rotational motion seismogram.

$$m_{ij}^{expl}(\mathbf{r},\tau) = \Psi(\tau)\begin{bmatrix} 1 & 0 & 0 \\ 0 & 1 & 0 \\ 0 & 0 & 1 \end{bmatrix} \tag{5-1}$$

where

$$\Psi(\tau) = \Psi(\infty)\left(1 - e^{-kt}\left[1 + k\tau + \frac{(k\tau)^2}{2} + \frac{(k\tau)^3}{6} - B(k\tau)^4\right]\right) \tag{5-2}$$

And $\tau = t - r/\alpha$ is the reduced time, k controls the bandwidth of the source, and B controls the degree of overshoot. We defined the earthquake source tensor as

$$m_{ij}^{EQ}(\mathbf{r},\tau) = f(\tau)\begin{bmatrix} -0.3584 & 0.1631 & -0.8623 \\ 0.1631 & 0.1130 & -0.2717 \\ -0.8623 & -0.2717 & 0.2454 \end{bmatrix} \tag{5-3}$$

which simulates a fault with a strike of 45°, a dip of 19°, and a rake of 32°. The source time function for the earthquake source is given by

$$f(t) = m\left(\frac{2}{d}t\right)^{1+\gamma} \quad \text{for } 0 \le t \le \frac{d}{2} \tag{5-4}$$

and

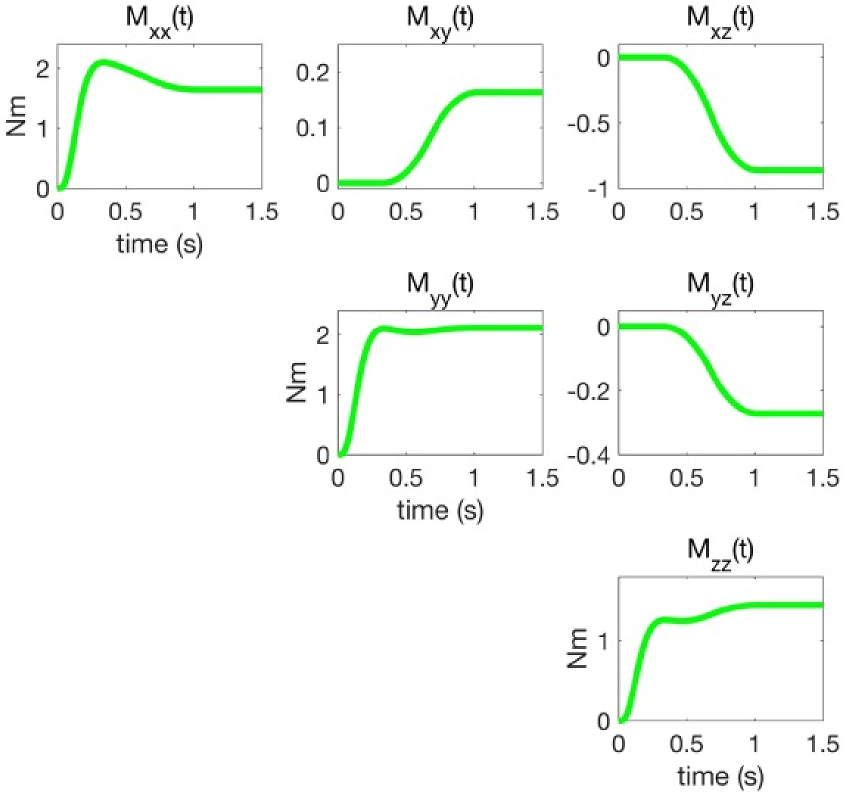

Figure 5-2: The source time functions corresponding the moment tensor used to simulate the data.

$$f(t) = M_0 \left(2 - \frac{2}{d}t\right)^{1+\gamma} \quad \text{for } \frac{d}{2} \le t \le d \tag{5-5}$$

where M_0 is the maximum amplitude, d is the total time of $f(t)$, and γ controls the shape of the function (Tanioka and Ruff, 1997). Thus, the source model used to create the synthetic data is a linear combination of two sources defined above:

$$M_{ij}(\mathbf{r}, t) = m_{ij}^{EQ}(\mathbf{r}, t) + m_{ij}^{expl}(\mathbf{r}, t) \tag{5-6}$$

which is shown in Figure 5-2.

Using the source defined in Equation 5-6, we simulated the full wavefield through the model and recorded it on the sixteen stations shown in Figure 5-1. At each station, three components of translational surface velocity,

$$\mathbf{v}(\mathbf{r}', t) = \begin{bmatrix} v_x(\mathbf{r}', t) \\ v_y(\mathbf{r}', t) \\ v_z(\mathbf{r}', t) \end{bmatrix} \tag{5-7}$$

and three components of rotational rate motion,

$$\boldsymbol{\Omega}(\mathbf{r}', t) = \begin{bmatrix} \omega_x(\mathbf{r}', t) \\ \omega_y(\mathbf{r}', t) \\ \omega_z(\mathbf{r}', t) \end{bmatrix} \tag{5-8}$$

are recorded. For the translational seismograms, the subscript indicates the direction of motion, and for the rotational rate motions seismograms, the subscript indicates the axis about which the rotation occurs. Note that in a field setting, the rotational motions would most likely be estimated using the gradiometric method described in the previous chapter; however, there are dedicated rotational sensors (e.g. Lee et al., 2009). For our simulations, however, our finite difference wave simulator can compute (and output) the gradient or rotation rate of the wavefield directly, of which we use the latter for simulations shown in this report.

5.2. Green's Functions

Recall that seismic Green's functions (GFs) are the impulse response of the Earth. As such, we can estimate the required GFs by using the same geologic model, array configuration, and finite difference wave simulator as for the synthetic data. The primary difference is the input source: for GFs the source is an impulse, which we implement numerically with a delta function. Note that we must compute the GFs for each term in the moment tensor. Specifically, for the M_{xx} component GF, we define the source as

$$GF_{xx}(\mathbf{r}', t'; \mathbf{r}, t) = \delta(t) \begin{bmatrix} 1 & 0 & 0 \\ 0 & 0 & 0 \\ 0 & 0 & 0 \end{bmatrix} \tag{5-9}$$

where $\delta(t)$ is a discrete Dirac delta function with amplitude $\frac{1}{\Delta t}$ at $t = 0$ and zero amplitude elsewhere. Likewise for the M_{xy} component GF, the source is defined as

$$GF_{xy}(\mathbf{r}', t'; \mathbf{r}, t) = \delta(t) \begin{bmatrix} 0 & 1 & 0 \\ 1 & 0 & 0 \\ 0 & 0 & 0 \end{bmatrix} \tag{5-10}$$

and so on. Note that for the GFs that correspond to off-diagonal components of the moment tensor, symmetry is preserved. We compute six sets of GFs, one for each component of the moment tensor, and each set of GFs (corresponding to a single moment tensor component) contains six total components of motion: three directions of translational velocity and three directions of rotation rate. Thus, for each station of the (synthetic) array there are 36 total 'channels' of GFs: (three components of translational velocity) plus (three components of rotational motion) by (six terms in the moment tensor).

5.3. Inversion

The simulated data contains three components of translation and rotational seismograms for each station (Figures 5-3 and 5-4). However, we note that the amplitude (with units of m/s) of the translational velocity seismograms are approximately two orders of magnitude higher than that of the rotational rate motions seismograms (with units of radians/second). If we were to use the raw

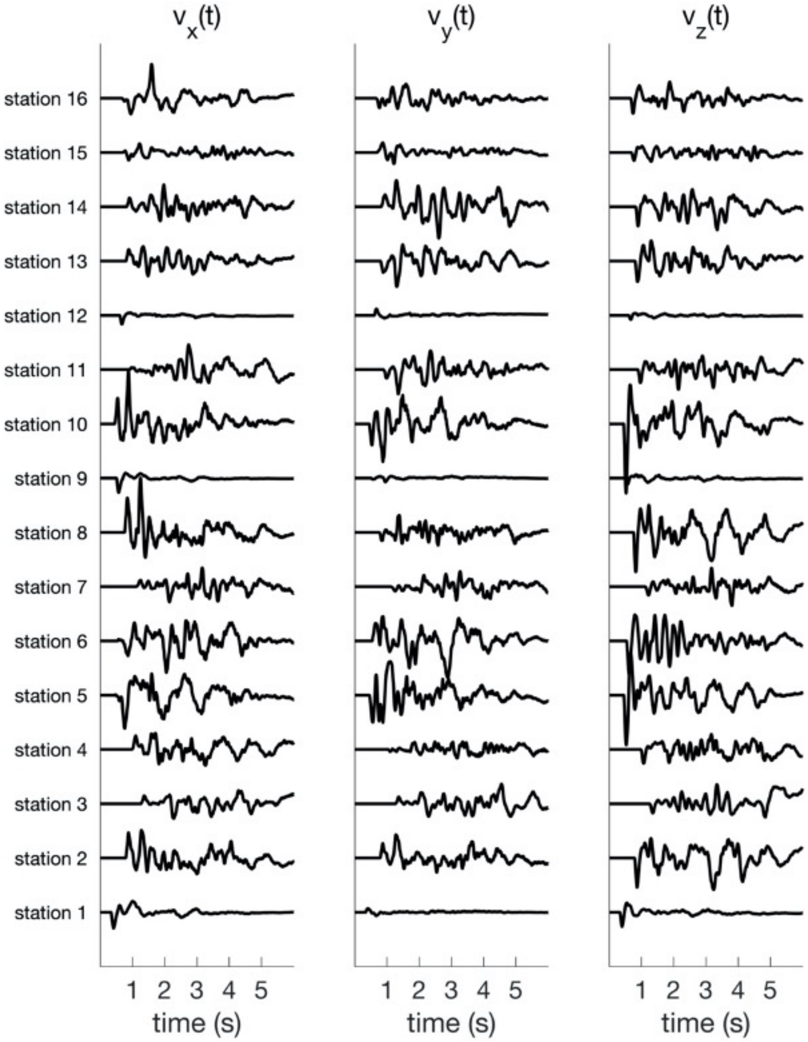

Figure 5-3: Unfiltered, synthetic, translation velocity seismograms. The three panels correspond to $v_x(t)$, $v_y(t)$, and $v_z(t)$. All of the seismograms are normalized to the maximum amplitude of the entire suite of translational seismograms, and are thus shown in their correct relative amplitude.

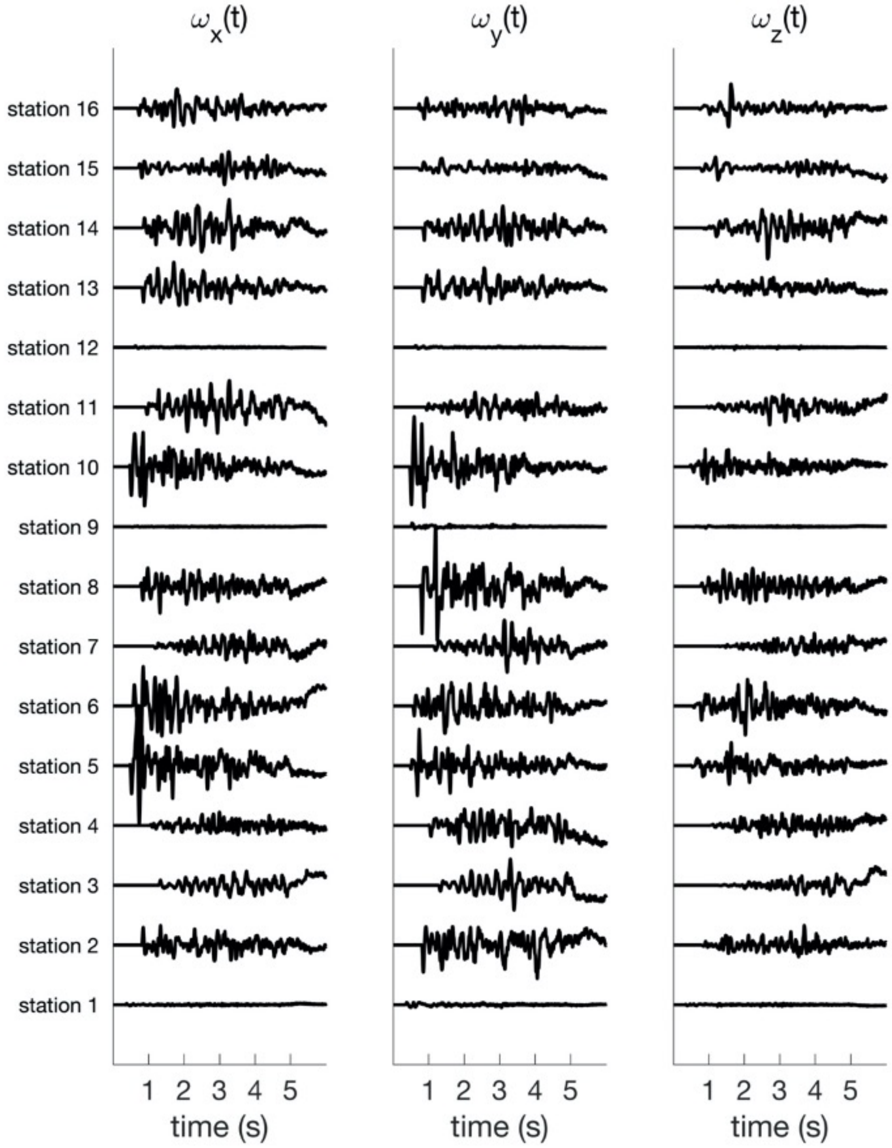

Figure 5-4: Same as Figure 5-3, but for the rotational rate motion seismograms.

translational and rotational data (and their corresponding GFs) in an inversion directly, the solution would be dominated by the translational motion data. Thus, we "non-dimensionalize" both the data and GFs prior to inverting by dividing by scalars with the appropriate units. Specifically, we normalize the data and GFs by dividing by the root-mean-square (RMS) amplitude of the appropriate data type:

$$\begin{bmatrix} \begin{pmatrix} | \\ \frac{v}{\alpha} \\ | \end{pmatrix} \\ \begin{pmatrix} | \\ \frac{\Omega}{\beta} \\ | \end{pmatrix} \end{bmatrix} = \begin{bmatrix} \begin{pmatrix} | \\ \frac{G\{v\}}{\alpha} \\ | \end{pmatrix} \\ \begin{pmatrix} | \\ \frac{G\{\Omega\}}{\beta} \\ | \end{pmatrix} \end{bmatrix} \mathbf{m}$$

where α is the mean RMS amplitude of all of the translational component data and β is the mean RMS amplitude of all the rotational component data. Because we apply these scalars to both sides of the equation, the amplitude of **m** is unaffected.

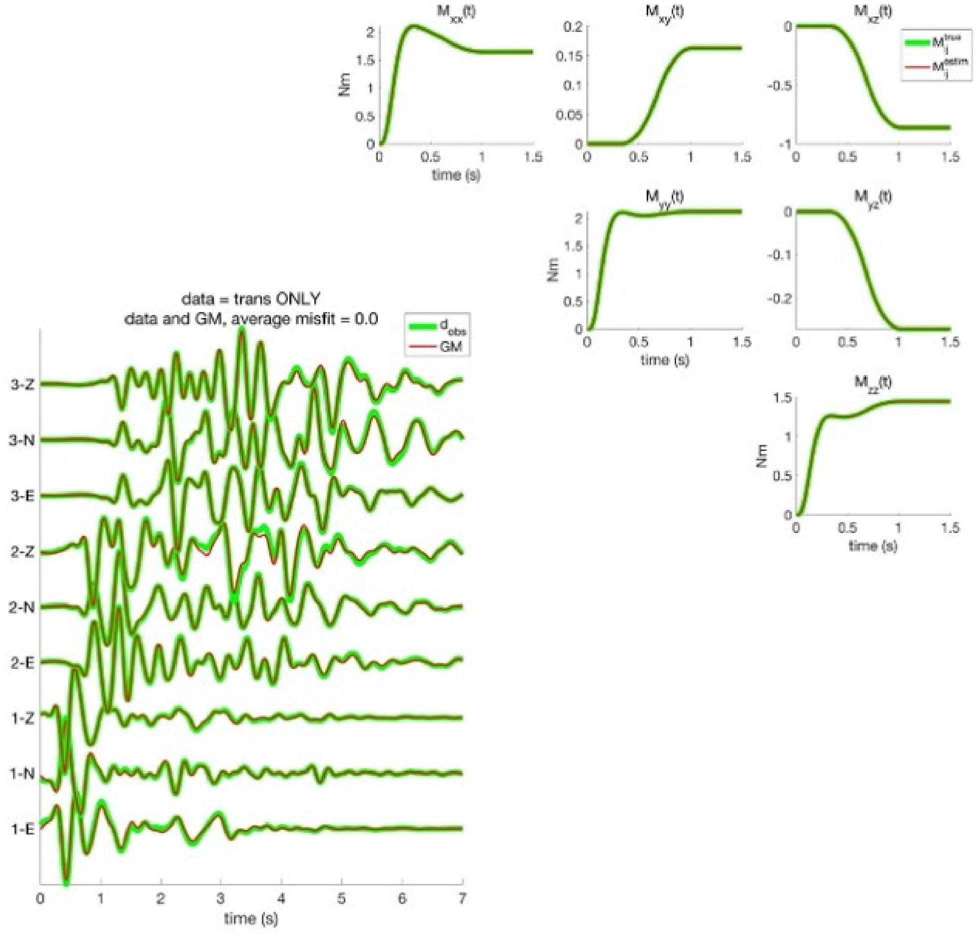

Figure 5-5: Results of inverting the translational data only. The top panel shows the true seismic source functions in green and the estimated seismic source functions in red. The bottom panel shows the fit-to-data: the green are the observed (synthetic) data and the red are the data predicted by the inversion. Note that for clarity, we only show the data for the first three stations of the array.

5.4. Numerical Tests and Examples

In this section we show the results of inverting the synthetic data. We developed computer codes to implement our inversion using the Matlab programming language. The codes are constructed such that we can easily define which stations and channels of data we use in the inversions: we can easily include or omit any channel or component of translational or rotational data. This capability was implemented with the future goal of testing the benefits and/or limitations of including rotational motion data when inverting for time-domain moment tensors. However, the results presented here are only to demonstrate the validity of our mathematical model and the efficacy of our inversion method. We do not perform a detailed study of the resolution, the effects of model and/or data uncertainty, or the benefits (or issues) associated with the inclusion of rotational motion seismograms to this type of inversion. These types of experiments and analysis are outside the scope of this report, but do serve as the topic of ongoing and future study.

For the first example, we show the results of inverting only the translational velocity data (Figure 5-5). This test serves as benchmark test: previous analysis by us (and others) typically use only

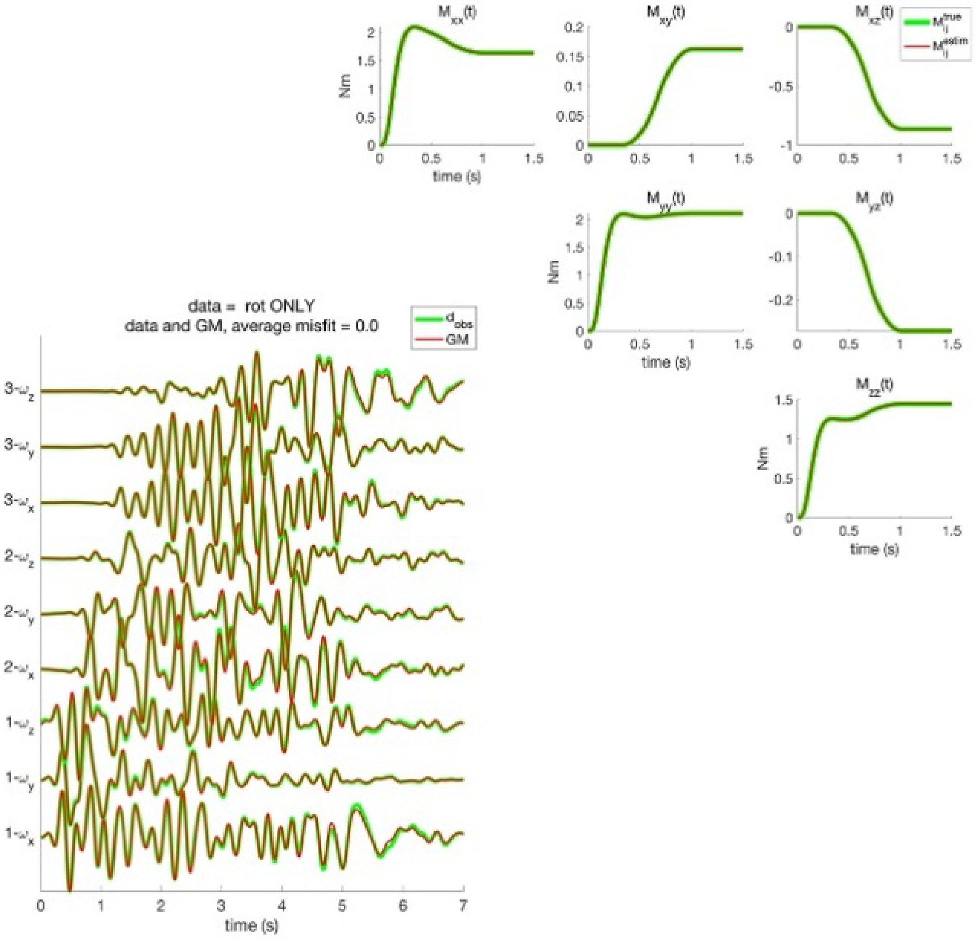

Figure 5-6: The results of our inversion where only the rotational motion data are inverted. Note that the seismic source functions are nearly perfectly recovered (top panel), and the fit-to-data is nearly perfect (bottom panel). For clarity, only the rotational motion seismograms for the first three stations in the array are shown.

translation velocity seismograms for analysis. Note that the inversion perfectly recovers the source model and the fit to data is almost perfect. This is to be expected for perfect, noise free, synthetic data. The fit-to-data is computed by using the estimated seismic source functions, shown in red in the top panel of Figure 5-5, and convolving them with the GFs according to Equation 4-10. The misfit is defined as the difference between the observed data and the predicted data:

$$\epsilon = \frac{(\mathbf{d} - \mathbf{Gm})^T(\mathbf{d} - \mathbf{Gm})}{\mathbf{d}^T\mathbf{d}} \tag{5-11}$$

where **d** is the observed data that we invert (which is in case synthetic), **G** are the GFs, and **m** is seismic source functions estimated from our inversion. Note that for the results shown in Figure 5-5, the misfit is zero.

For the next test, we invert only the rotational motion seismograms, and obtain results that are similar to those shown in Figure 5-5: perfectly recovered seismic source functions and a nearly perfect fit to data (Figure 5-6).

As a final test, we inverted both translational velocity and rotational motion seismograms simultaneously (Figure 5-7). However, we only selected the seismograms from three of the array stations. In this case, the estimated seismic source functions were nearly identical to the actual seismic source functions, (i.e. they look identical to those shown in Figures, 5-5 and 5-6), and thus we don't show them here. However, the misfit is 0.08, which indicates that the fit isn't perfect. However, this is likely because we are using only three stations of data (albeit six channels for each station, for a total of eighteen total channels of data), and, thus, we are not densely enough sampling

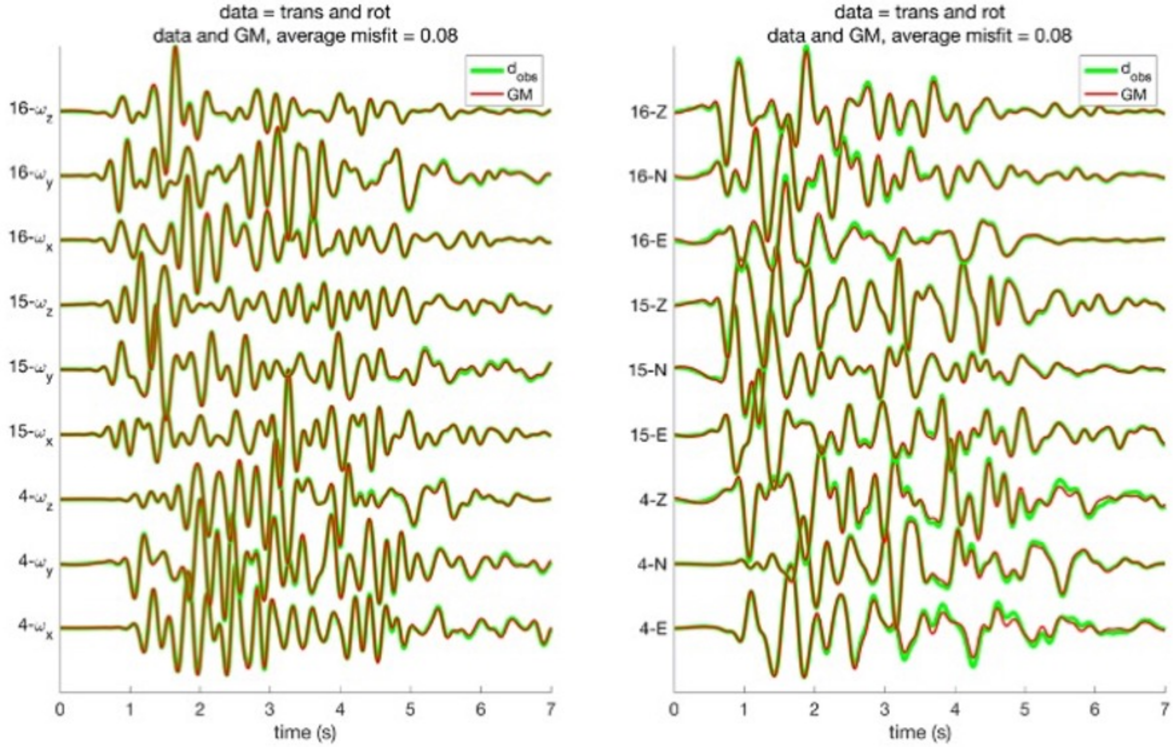

Figure 5-7: The fit-to-data for the case where we simultaneously invert both translational and rotational seismograms. However, we only selected the data from three stations in the array. For this test, the translational and rotational motion seismograms are collected from array stations that are co-located.

the focal sphere of the source. Regardless, we conducted this test to verify that our inversion code is correctly estimating the seismic source parameters and that we can easily select arbitrary channels of data, whether they be translational or rotational.

5.5. Concluding Remarks

In Chapter 4 we presented a method to invert translational and rotational motion seismograms for the seismic source functions that correspond to the seismic moment tensor. Our code correctly recovers the seismic source model in synthetic tests, indicating that our mathematical model and implementation are correct. Additionally, we've designed our code so that it's easy to select which stations and data components to invert.

We were motivated to include rotational motion seismograms in an inversion for seismic source functions for two reasons. First, there is evidence in the literature that including rotational motions can increase the accuracy and precision of seismic source estimates. However, much of this previous work made different model assumptions than we do. For example, the work of Bernauer and Fichtner (2014) and Reinwald et al. (2016) showed that including rotational seismic motions increases the resolution of finite source models. In the case of point source models, Donner et al. (2016) and Ichinose et al. (2020) also showed an increase in source resolution, but they inverted only for centroid moment tensor components, where source depth was a free parameter: i.e. they assume that the source time function for all of the force couples is identical, and thus they only invert for the six scalar values of the tensor (in addition to the source depth). Our inversion differs from these previous efforts in two important ways. First, we assume a point source where we have perfect knowledge of the source location. Secondly, and perhaps most importantly, we do not impose the condition that all of the source time functions for all the tensor components are similar. Rather, we allow each seismic source function for each tensor component to have independent time histories. This model may be more appropriate for explosion monitoring tasks, as it's feasible that two distinct seismic mechanisms can be present when buried explosions are detonated: the nearly-isotropic explosion source which can then be followed by a double-couple type of source that represents the release of pre-existing tectonic stress. Thus the inversion scheme we describe here may improve monitoring efforts by allowing a time-variable decomposition of the seismic source, which is something that almost no current source inversion schemes allow.

This page left blank

6. SUMMARY

We have discussed two new software enhancements in this report: the 3-D TVBC and the addition of seismic gradiometer data to full waveform moment tensor inversions. We derive the theory and discuss some numerical implementation aspects of both enhancements. Additionally, we demonstrate both additions in action with examples and comparisons to expected behavior, which validate the methods and software implementations.

For the 3-D TVBC simulations, we showed that in a 3-D model that adheres to the 2D-C assumptions the TVBC is nearly transparent to the propagating wavefield, with very good agreement with expectations. We also tested the new TVBC implementation in a 3-D model that does not adhere to the 2D-C assumptions that were used in making the TVBC with CTH. In this case, the artifacts were noticeable, as expected, but still relatively small in amplitude compared to the true 3-D wavefield. None of the main seismic phases were greatly impacted by the artifacts. Thus, in certain cases, faster 2D-C simulations can be used for the nonlinear portion of the modeling while full 3-D modeling is used in the linear regime to get reasonable estimates of the 3-D wavefield produced from a nonlinear source. Obviously, this approach only will be feasible if the near-source region can be approximated as 2D-C. An even computationally faster approach exists if a linear source equivalent model is available for the source in question. In this case, the 3-D TVBC is not required, and a simple point seismic moment tensor source that utilizes the linear source equivalent source time functions can be used without need for a nonlinear simulation. We showed that the wave fields produced when using a 3-D TVBC are visually identical to those produced when the linear source equivalent source was used without the 3-D TVBC artifacts.

We also derived and implemented full waveform moment tensor source inversions that allows gradiometer-derived observations to be combined with traditional linear translational seismic recordings. This permits exploration of the potential advantages of using the six degrees of freedom of the wavefield available in a full 2-D (surface) gradiometer deployment instead of the three degrees of freedom available in typical 3-C translational component seismic data. We demonstrated that the implementation of the inversion scheme produces expected and virtually perfect results when the focal sphere is sufficiently sampled. Even in the case with incomplete sampling of the focal sphere, we are able to recover the known source time functions nearly perfectly with very small misfit. The tests we show here are designed only to show the efficacy of our method. On-going and future research efforts are aimed at 1) determining whether including rotational motions increase the accuracy and/or precision of the time-varying seismic source functions when the model and/or data contain uncertainties, 2) error propagation, and 3) how to best incorporate rotational motions in a field setting.

This page left blank

REFERENCES

1. Aki, K., and P.G. Richards (2002). *Quantitative Seismology*, Second Edition, University Science Books, Sausalito, CA.
2. Bernauer, M., A. Fichtner, and H. Igel (2009). Inferring Earth structure from combined measurements of rotational and translational ground motions, *Geophysics*, 74, WCD41-WCD47.
3. Bernauer, M., and A. Fichtner (2014). Reducing nonuniqueness in finite source inversion using rotational ground motions, *J. Geophys. Res. Solid Earth*, 119, 4860-4875.
4. Donner, S., M. Bernauer, and H. Igel (2016). Inversion for seismic moment tensors combining translational and rotational ground motions, *Geophys. J. Int.*, 207, 562-570.
5. Haskell, N.A., (1967). Analytic Approximation for Elastic Radiation from a Contained Underground Explosion, *J. Geophys. Res.*, **72**(10), 2583-2587.
6. Ichinose, G.A., S.R. Ford, and R.J. Mellors (2020). Regional Moment Tensor Inversion using Rotational Observations, *J. Geophys. Res. Solid Earth*, 126, e2020JB020827.
7. Komatitsch, D., and R. Martin (2007). An Unsplit Convolutional Perfectly Matched Layer Improved at Grazing Incidence for the Seismic Wave Equation, *Geophysics*, **72**(5), SM155-SM167, dos 10.1190/1.2757586.
8. Langston, C.A., (2007a). Spatial Gradient Analysis for Linear Seismic Arrays, *Bull. Seis. Soc. Am.*, 97, 265-280.
9. Langston, C.A., (2007b). Wave Gradiometry in Two Dimensions, *Bull. Seis. Soc. Am.*, 97, 401-416.
10. Langston, C.A., (2007c). Wave Gradiometry in the Time Domain, *Bull. Seis. Soc. Am.*, 97, 926-933.
11. Lee. W.H.K., H. Igel, and M.D. Trifunac (2009). Recent Advances in Rotational Seismology. *Seis. Res. Lett.*, **80**(3), 479-490.
12. Liang, C., and C.A. Langston (2009). Wave Gradiometry for USArray: Rayleigh waves, *J. Geophys. Res.,* **114**(B2). doi:10.1029/2008JB005918.
13. Moczo, P., J. Kristek, V. Vavrycuk, R.J. Archuleta, and L. Halada (2002). 3D heterogeneous staggered-grid finite-difference modeling of seismic motion with volume harmonic and arithmetic averaging of elastic model and densities. *Bull. Seis. Soc. Am.*, 92, 3042-3066.
14. Mueller, R.A., and J.R. Murphy (1971). Seismic Characteristics of Underground Nuclear Explosions, Part I. Seismic Spectrum Scaling, *Bull. Seis. Soc. Am.*, **61**(6), 1675-1692.
15. Murphy, J.R., (1977). Seismic Source Functions and Magnitude Determinations for Underground Nuclear Detonations, *Bull. Seis. Soc. Am.*, 67(1), 135-158.
16. Poppeliers, C., (2010). Seismic Wave Gradiometry Using the Wavelet Transform: Application to the Analysis of Complex Surface Waves Recorded at the Glendora Array, Sullivan, Indiana, USA., *Bull. Seis. Soc. Am.*, 100, 1211-1224.
17. Poppeliers, C., (2011). Multiwavelet Seismic-Wave Gradiometry, *Bull. Seis. Soc. Am.*, 101, 2108-2121.
18. Poppeliers, C., and E.V. Evans (2015). The Effects of Measurement Uncertainties in Seismic-Wave Gradiometry, *Bull. Seis. Soc. Am.*, 105, 3143-3155.
19. Poppeliers, C., and L. Preston (2020). The effects of model uncertainty on the inversion of seismic data for seismic source functions, *Geophys. J. Int.*, **224**(1), 100-120.

20. Poppeliers, C., and P. Punosevac (2013). Three-Dimensional Wave Gradiometry for Polarized Seismic Waves, *Bull. Seis. Soc. Am.*, 103, 2161-2172.
21. Poppeliers, C., P. Punosevac, and T. Bell (2013). Three-Dimensional Seismic-Wave Gradiometry for Scalar Waves, *Bull. Seis. Soc. Am.*, 103, 2151-2160.
22. Poppeliers, C., Wheeler, L.B., and L. Preston (2020). The Effects of Atmospheric Models on the Estimation of Infrasonic Source Functions at the Source Physics Experiment, *Bull. Seis. Soc. Am.* **110**(3), 998-1010.
23. Preston, L.A. (2017). *Nonlinear to Linear Elastic Code Coupling in 2-D Axisymmetric Media*, SAND2017-8848, Sandia National Laboratories, Albuquerque, NM.
24. Preston, L., M. Eliassi, and C. Poppeliers (2021). *Programmatic Advantages of Linear Equivalent Seismic Models*, SAND2021-10201, Sandia National Laboratories, Albuquerque, NM.
25. Reinwald, M., M. Bernauer, H. Igel, and S. Donner (2016). Improved finite-source inversion through joint measurements of rotational and translational motions: A numerical study, *Solid Earth*, 7, 1467-1477, doi: 10.5194/se-7-1467-2016.
26. Schmitt, G., D.A. Crawford, E.N. Harstad, D.M. Hensinger, and K.P. Ruggirello, (2017). *CTH User's Manual and Input Instructions, Version 12.0, CTH Development Projects*, Sandia National Laboratories, Albuquerque, NM, April 20, 2017 (OUO).
27. Stump, B.W., and L.R. Johnson (1977). The determination of source properties by the linear inversion of seismograms, *Bull. Seis. Soc. Am.*, 67, 1489-1502.
28. Tanioka, R., and L.J. Ruff (1997). Source Time Functions, *Seism. Res. Lett.*, **68**(3), 386-400.

DISTRIBUTION

Email—Internal

Name	Org.	Sandia Email Address
Lauren Wheeler	08913	lwheele@sandia.gov
Stephanie Teich-McGoldrick	06756	steichm@sandia.gov
Stephanie Eras	06756	sjeras@sandia.gov
Technical Library	01977	sanddocs@sandia.gov

This page left blank

This page left blank